*J. Fluid Mech.* (2004), *vol.* 513, *pp.* 309–341.  
DOI: 10.1017/S0022112004000060 Printed in the United Kingdom

# A numerical study of crescent waves

By DAVID R. FUHRMAN, PER A. MADSEN AND HARRY B. BINGHAM

Department of Mechanical Engineering, Technical University of Denmark, DK-2800 Kgs. Lyngby, Denmark

(Received 21 August 2003 and in revised form 16 February 2004)

In this paper, a high-order Boussinesq model is used to conduct a systematic numerical study of crescent (or horseshoe) water wave patterns in a tank, arising from the instability of steep deep-water waves to three-dimensional disturbances. The most unstable phase-locked (L2) crescent patterns are investigated, and comparisons with experimental measurements confirm the quantitative accuracy of the model. The unstable growth rate is also investigated, as are the effects of variable nonlinearity. The dominant physical mechanism is clearly demonstrated (through time and space series analysis) to be the established quintet resonant interaction, involving the primary wave with a pair of symmetric satellites. A numerical investigation into oscillating crescent patterns is also included, and a detailed account of the complicated oscillation cycle is presented. These patterns are shown to arise from quintet resonant interactions involving the primary wave with two unsymmetric satellite pairs. Pre-existing methods for analysing the stability of steep deep-water plane waves subject to three-dimensional perturbations are extended to provide accurate quantitative estimates for the oscillation period. A possible explanation for their selection in experiments is also provided. Finally, we use the model to conduct a series of experiments involving competition between various unstable modes. The results generally show that multiple instabilities can grow simultaneously, provided that they are of roughly equivalent strength. Results using random perturbations also match observations in physical experiments both in the form (i.e. two- or three-dimensional) and the location of the initial instability. The computational results are the first examples of highly nonlinear (to the breaking point) deep-water wave modeling in two horizontal dimensions with a Boussinesq model. The efficiency of the model has allowed for a quantitative study of these phenomena at significantly larger spatial and temporal scales than have been demonstrated previously, providing new insight into the complicated physical processes involved.

## 1. Introduction

This work presents a numerical study of the fascinating phenomenon of 'crescent' or 'horseshoe' water wave patterns, which occur readily on the sea surface, e.g. from the action of a fresh wind (examples in nature can be seen in the photographs of Shrira, Badulin & Kharif 1996). Such patterns have been observed experimentally in wave tanks in the absence of wind in Melville (1982), Su (1982) and Su *et al.* (1982), as well as in its presence in Kusaba & Mitsuyasu (1986) and Collard & Caulliez (1999). As noted in Annenkov & Shrira (1999), the patterns are very important in ocean science, since they modify the airflow above the surface and thus affect the air–sea momentum transfer, while also changing in a specific way radar scattering

from the sea surface (Shrira, Badulin & Voronovich 2000). Furthermore, conceptually new models for statistically describing wind-wave field dynamics become necessary in their presence (Shrira *et al.* 1996). Such patterns are of additional interest in nonlinear science (Annenkov & Shrira 1999). They are also important in engineering, as they are part of the natural evolution of steep deep-water wavetrains, which are commonly used as design waves for ships and other offshore structures.

The inception mechanism is generally acknowledged to be the class II (three-dimensional) instability of McLean (1982) (see also McLean *et al.* 1981), who numerically analysed the stability of steep deep-water wavetrains subject to periodic disturbances. The dominant physical processes have also been confirmed as quintet resonant interactions using the qualitative model of Shrira *et al.* (1996), based on a modified Zakharov equation. An investigation using the model of Dommermuth & Yue (1987) can also be found in Skandrani (1997). Additional qualitative studies into the long-term sporadic nature of crescent waves can be found in Annenkov & Shrira (1999, 2001). While the two-dimensional (Benjamin & Feir 1967), class I instability is well understood, quantitative investigations into the three-dimensional class II instability are rare. This is probably a consequence of the high computational costs associated with the three-dimensional nature of the patterns in combination with the high nonlinearity at which they occur. Numerical simulations with a boundary-element model (Xue *et al.* 2001) have, however, demonstrated quantitatively accurate crescent forms, arising naturally from the nonlinear evolution of a perturbed plane incident wave. This ground-breaking investigation is limited to relatively small domains and short time scales, making detailed investigations into the physical processes difficult.

Largely inspired by this work, the present paper contains a more extensive fully nonlinear numerical study of the class II instabilities leading to crescent wave patterns on the free surface. We use a numerical model based on the fully nonlinear and highly dispersive Boussinesq formulation of Madsen, Bingham & Liu (2002) and Madsen, Bingham & Schäffer (2003). We consider significantly larger spatial and temporal scales than in Xue *et al.* (2001), paying particular attention to the complicated physical processes involved in each of the simulations presented. First, we investigate the most common phase-locked L2 patterns (as denoted in Su 1982; Su *et al.* 1982). The model is verified both qualitatively and quantitatively through comparison with experimental measurements. Detailed investigations into the unstable growth rate, the effects of nonlinearity, as well as the physical processes involved during the crescent wave evolution to breaking are also provided. Secondly, we present a detailed numerical investigation into the more recently observed oscillating crescent wave patterns. Through direct numerical simulation we obtain excellent qualitative and quantitative agreement with the oscillating forms observed by Collard & Caulliez (1999), while also demonstrating distinct L3 and L4 crescent patterns noted in Su *et al.* (1982) and Su (1982). Furthermore, the stability analysis of McLean (1982) is extended, resulting in a quantitative explanation for each of the oscillating cases considered. A possible explanation for their selection in the experiments is also provided. Finally, we present a series of numerical experiments involving the competition of various unstable modes during their initial growth to the breaking point. These include competition between isolated symmetric (phase-locked) and unsymmetric (oscillating) class II modes, between isolated class I and II modes, as well as with random (white noise) disturbances.

The remainder of the paper is organized as follows. The Boussinesq formulation and its numerical solution are outlined in § 2, with § 3 describing the periodic perturbation of steady plane waves used to generate the crescent patterns. The dominant (L2)

phase-locked crescent patterns are investigated both qualitatively and quantitatively in § 4. The different, but related oscillating patterns are investigated in § 5. A series of numerical experiments involving the competition of various unstable modes is presented in § 6. The issue of computational efficiency is addressed in § 7. Finally, conclusions are drawn in § 8.

## 2. The Boussinesq model

In this section, we provide a review of the Boussinesq formulation derived by Madsen *et al.* (2002, 2003). Consider the flow of an incompressible, inviscid fluid with a free surface. A Cartesian coordinate system is adopted, with the $x$- and $y$-axis located on the still-water plane, and with the $z$-axis pointing vertically upwards. The fluid domain is bounded by the sea bed at $z=-h(\boldsymbol{x})$, with $\boldsymbol{x}=\langle x, y\rangle$, and the free surface at $z=\eta(\boldsymbol{x}, t)$, where $t$ is time. It is computationally convenient to express the free-surface conditions in terms of velocity variables at the free surface (see e.g. Zakharov 1968; Madsen *et al.* 2002, 2003). This leads to the following expressions for the kinematic and dynamic free-surface conditions

$$\frac{\partial \eta}{\partial t}=\tilde{w}\,(1+\nabla\eta\cdot\nabla\eta)-\tilde{\boldsymbol{U}}\cdot\nabla\eta, \tag{2.1}$$

$$\frac{\partial \tilde{\boldsymbol{U}}}{\partial t}=-g\nabla\eta-\nabla\left(\frac{\tilde{\boldsymbol{U}}\cdot\tilde{\boldsymbol{U}}}{2}-\frac{\tilde{w}^2}{2}(1+\nabla\eta\cdot\nabla\eta)\right), \tag{2.2}$$

where

$$\tilde{\boldsymbol{U}}=\langle\tilde{U}, \tilde{V}\rangle=\tilde{\boldsymbol{u}}+\tilde{w}\nabla\eta. \tag{2.3}$$

Here, $\tilde{\boldsymbol{u}}=\langle\tilde{u}, \tilde{v}\rangle$ and $\tilde{w}$ are the horizontal and vertical velocities directly on the free surface, $g=9.81\ \mathrm{m\,s^{-2}}$ is the acceleration due to gravity, and $\nabla=\langle\partial/\partial x, \partial/\partial y\rangle$ is the horizontal gradient operator. Evolving $\eta$ and $\tilde{\boldsymbol{U}}$ forward in time requires a means of computing the associated $\tilde{w}$, subject to the Laplace equation and the kinematic bottom condition

$$w+\nabla h\cdot\boldsymbol{u}=0,\quad z=-h(\boldsymbol{x}). \tag{2.4}$$

For this purpose, the Boussinesq method derived by Madsen *et al.* (2002, 2003) is adopted (see also Madsen & Agnon 2003). This method applies a truncated, Padé-enhanced Taylor series expansion of the velocity potential about an arbitrary level $z=\hat{z}$ in the fluid. In addition, the vertical component of velocity at this level is retained as an unknown, leading to an extremely accurate method (applicable to $kh\approx 25$ for surface quantities and $kh\approx 12$ for vertical velocity distributions). Thus, the vertical distribution of fluid velocity is approximated by

$$\boldsymbol{u}(\boldsymbol{x}, z, t)=(1-\alpha_2\nabla^2+\alpha_4\nabla^4)\hat{\boldsymbol{u}}^*(\boldsymbol{x}, t)+((z-\hat{z})\nabla-\beta_3\nabla^3+\beta_5\nabla^5)\hat{w}^*(\boldsymbol{x}, t), \tag{2.5}$$

$$w(\boldsymbol{x}, z, t)=(1-\alpha_2\nabla^2+\alpha_4\nabla^4)\hat{w}^*(\boldsymbol{x}, t)-((z-\hat{z})\nabla-\beta_3\nabla^3+\beta_5\nabla^5)\hat{\boldsymbol{u}}^*(\boldsymbol{x}, t), \tag{2.6}$$

where

$$\left.\begin{aligned}\alpha_2&=\frac{(z-\hat{z})^2}{2}-\frac{\hat{z}^2}{18},\ \alpha_4=\frac{(z-\hat{z})^4}{24}-\frac{\hat{z}^2(z-\hat{z})^2}{36}+\frac{\hat{z}^4}{504},\\ \beta_3&=\frac{(z-\hat{z})^3}{6}-\frac{\hat{z}^2(z-\hat{z})}{18},\ \beta_5=\frac{(z-\hat{z})^5}{120}-\frac{\hat{z}^2(z-\hat{z})^3}{108}+\frac{\hat{z}^4(z-\hat{z})}{504}.\end{aligned}\right\} \tag{2.7}$$

In (2.5) and (2.6), the quantities $\hat{\boldsymbol{u}}^*$ and $\hat{w}^*$ are pseudo-velocity variables which have been introduced to allow Padé enhancement of the Taylor series operators. Optimal velocity distributions are obtained near $\hat{z} = -h/2$, and we adopt this value throughout.

Inserting (2.5) and (2.6) into (2.4) and setting $\nabla h = 0$ gives the following expression of the kinematic bottom condition

$$\left(1 - \tfrac{4}{9}\gamma^2\nabla^2 + \tfrac{1}{63}\gamma^4\nabla^4\right)\hat{w}^* + \left(\gamma\nabla - \tfrac{1}{9}\gamma^3\nabla^3 + \tfrac{1}{945}\gamma^5\nabla^5\right)\hat{\boldsymbol{u}}^* = 0, \tag{2.8}$$

where $\gamma = (h + \hat{z})$. It is straightforward to include the variable bottom terms, as in Madsen *et al.* (2002, 2003), however, since they are not used in this work, the presentation will be simplified to a flat bottom. Combining (2.8) with (2.5) applied at $z = \eta$, while also invoking (2.3) gives a system of partial differential equations (PDEs) that can be solved for $\hat{\boldsymbol{u}}^*$ and $\hat{w}^*$ in terms of $\tilde{\boldsymbol{U}}$ and $\eta$. Fuhrman & Bingham (2004) have shown that under the additional assumption of potential (irrotational) flow such that

$$\frac{\partial u}{\partial y} - \frac{\partial v}{\partial x} = 0, \tag{2.9}$$

the system simplifies significantly, and we solve this irrotational form here. Note that (2.9) is a single component of the vorticity vector, and that the other elements (involving $z$-derivatives) have already been eliminated via the expansion of the velocity potential in the $z$-direction. The resulting discrete linear system is hereinafter referred to as $\boldsymbol{A}\boldsymbol{x} = \boldsymbol{b}$. The matrix $\boldsymbol{A}$ is generally ill-conditioned, and a number of preconditioning strategies designed to enhance the convergence of iterative solutions for this specific problem can be found in Fuhrman & Bingham (2004). Having solved for the pseudo-velocity variables $\hat{\boldsymbol{u}}^*$ and $\hat{w}^*$, $\tilde{w}$ is computed from (2.6) applied at $z = \eta$, which closes the problem.

This system of PDEs is solved numerically using 37-point finite-difference approximations (as described in Fuhrman & Bingham 2004). Combined Dirichlet and Neumann boundary conditions are used to create closed boundaries on a rectangular domain. These conditions are imposed simply by reflecting the finite-difference coefficients evenly for Neumann boundary conditions and oddly for Dirichlet boundary conditions. The classical fourth-order four-stage explicit Runge–Kutta method is used for the time integration. Linear systems of the form $\boldsymbol{A}\boldsymbol{x} = \boldsymbol{b}$ are solved using an unrestarted GMRES (Saad & Schultz 1986) algorithm preconditioned with the matrix-free Fourier space preconditioner described in Fuhrman & Bingham (2004), which is extremely efficient for solving flat-bottom problems. All iterative solutions use a relative residual error tolerance $r = \|\boldsymbol{b} - \boldsymbol{A}\boldsymbol{x}\|_2 / \|\boldsymbol{b}\|_2$ of $10^{-6}$. A relaxation zone consisting of a single wavelength is used for the generation of waves at the left-hand boundary (as discussed in Madsen *et al.* 2002), with $x = 0$ defined as the end of this wavemaker region. Similarly, a relaxation zone consisting of 100 points is applied at the right-hand boundary to prevent reflection from the outgoing wave field.

## 3. Crescent wave generation

Crescent waves are generated in this work by superimposing the following three-dimensional perturbations

$$\eta' = \frac{\epsilon H}{2}\sin(k_x x - \omega' t + \beta)\cos(k_y y), \tag{3.1}$$

$$\tilde{\boldsymbol{U}}' = \tilde{\boldsymbol{u}}' + \tilde{w}'\nabla\eta, \tag{3.2}$$

where

$$\tilde{u}' = \frac{\epsilon\sqrt{gH}k_x}{2\left(k_x^2+k_y^2\right)^{1/4}}\sin(k_x x - \omega' t + \beta)\cos(k_y y)\exp\left(\sqrt{k_x^2+k_y^2}\eta\right), \tag{3.3}$$

$$\tilde{v}' = \frac{\epsilon\sqrt{gH}k_y}{2\left(k_x^2+k_y^2\right)^{1/4}}\cos(k_x x - \omega' t + \beta)\sin(k_y y)\exp\left(\sqrt{k_x^2+k_y^2}\eta\right), \tag{3.4}$$

$$\tilde{w}' = -\frac{\epsilon\sqrt{gH}}{2}\left(k_x^2+k_y^2\right)^{1/4}\cos(k_x x - \omega' t + \beta)\cos(k_y y)\exp\left(\sqrt{k_x^2+k_y^2}\eta\right), \tag{3.5}$$

over a streamfunction solution (Fenton 1988) for a plane wave travelling in the $+x$-direction, having a peak at $x=0$ at $t=0$. For the streamfunction solution, we set Stokes' drift (or mean fluid transport) velocity to $c_s=0$, to match the conditions of a closed flume. This plane incident wave has wavenumber $k_0$ and angular frequency $\omega_0$, with celerity $c=\omega_0/k_0$. In the above, a prime superscript corresponds to a perturbation of the previously defined base variables, with $\tilde{\boldsymbol{U}}' = \langle\tilde{U}', \tilde{V}'\rangle$ and $\tilde{\boldsymbol{u}}' = \langle\tilde{u}', \tilde{v}'\rangle$. The values $\langle k_x, k_y\rangle$ are the wavenumbers of the three-dimensional perturbation. The perturbations correspond to two superimposed travelling components with equal $k_x$ and opposite $k_y$ (resulting in a stationary standing wave structure in the $y$-direction). Unless otherwise noted, the generated perturbation is assumed to be bound to the unperturbed wave, having angular frequency

$$\omega' = \frac{k_x}{k_0}\omega_0. \tag{3.6}$$

This satisfies the condition that the wavemaker region is repeated every $(k_x/k_0-1)^{-1}$ basic periods.

This method of generation has been inspired by Xue *et al.* (2001), who used similar perturbations of the free surface and velocity potential over an exact plane Stokes wave in a boundary-element model. Their simulations used doubly periodic boundary conditions, thus the perturbations were applied only as initial conditions. Equations (3.1)–(3.5) generalize this idea to our particular time-stepping variables and time-variant wavemaker. In all simulations, the initial conditions are set to be this perturbed incident wave across the entire computational domain. Xue *et al.* (2001) found that the phase shift $\beta$ had no significant effect on the overall crescent development. We have confirmed this finding (provided that $\epsilon$ is sufficiently small), and throughout this paper we set $\beta=0$.

## 4. Phase-locked crescent patterns

### 4.1. *Model discretizations*

We begin the study of crescent waves by generating the common phase-locked (L2) patterns observed by Melville (1982), Su (1982), Su *et al.* (1982), Collard & Caulliez (1999), and others. The base incident wave throughout this paper corresponds to a streamfunction solution with $k_0=1$ m$^{-1}$ (i.e. with wavelength $L=2\pi/k_0=2\pi$ m). The spatial discretization in the $x$-direction is taken to be $\Delta x = L/40 = 0.1571$ m. For the water depth we use $h=L=2\pi$ m, giving an incident wave having $k_0h=2\pi$, i.e. well beyond the practical deep-water limit. The resulting discretizations for a number of nonlinearities used in this paper are given in table 1. Each case listed corresponds to the most unstable transversal class II mode according to McLean (1982) for the

| $H$ [m] | $H/L$ | $T$ [s] | $\omega_0$ [s$^{-1}$] | $\Delta t$ [s] | $k_y$ [m$^{-1}$] | $\Delta y$ [m] |
|---|---|---|---|---|---|---|
| 0.4021 | 0.064 | 1.972 | 3.186 | 0.04930 | 1.54 | 0.1275 |
| 0.5969 | 0.095 | 1.931 | 3.254 | 0.04828 | 1.33 | 0.1476 |
| 0.6032 | 0.096 | 1.929 | 3.257 | 0.04824 | 1.32 | 0.1488 |
| 0.6600 | 0.105 | 1.914 | 3.283 | 0.04786 | 1.23 | 0.1596 |
| 0.6974 | 0.111 | 1.903 | 3.302 | 0.04759 | 1.15 | 0.1707 |
| 0.7980 | 0.127 | 1.873 | 3.355 | 0.04682 | 0.79 | 0.2485 |
| 0.8231 | 0.131 | 1.865 | 3.369 | 0.04663 | 0.65 | 0.3021 |

TABLE 1. Discretizations used for crescent wave simulations with variable nonlinearity.

respective nonlinearities, and discretizations use $\Delta t = T/40$ (where $T$ is the basic period) and $\Delta y = L_y/32$. All simulations for a given nonlinearity throughout this paper use the parameters from table 1. We stress that each of the discretizations satisfy linear stability criteria (see the analysis of Fuhrman *et al.* 2004), with $\Delta t$ small enough to avoid potential dissipative effects from the time-stepping scheme. Throughout § 4, $k_x = 1.5k_0$ is used for the perturbation, with $\omega' = 1.5\omega_0$.

### 4.2. *The effects of smoothing filters on the growth rate*

Crescent waves are a highly nonlinear phenomena, and though the discretizations used are linearly stable, some form of dissipative interface is still generally necessary to maintain numerical stability. The resulting numerical instabilities (usually occurring as sawteeth at the wave crests) are due to the nonlinear terms, which tend to shift some eigenvalues of the discrete Jacobian matrix to the right half of the complex plane, as demonstrated locally in the numerical stability analysis of Fuhrman *et al.* (2004). There it is also shown that the system can be stabilized through the addition of relatively minor amounts of dissipation. Throughout this work, we apply Savitzky & Golay (1964) smoothing filters (see also Press *et al.* 1992) for this purpose, which have been used successfully in a number of other water wave studies (see e.g. Xue *et al.* 2001; Madsen *et al.* 2002; Fuhrman & Bingham 2004).

Although their use is commonplace, investigations into the relative effects of such smoothing filters are rarely presented. Our experience has shown, however, that it is important to recognize these effects, as they can have a profound influence on the solution, particularly on any higher harmonics which inevitably become important in nonlinear simulations. Here, we present one such investigation on the effects on the growth rate of the instability, ultimately leading to crescent wave formation. We consider waves with steepness $H/L = 0.105$ on a $513 \times 17$ grid, with $\epsilon = 0.16$. Because the crescent patterns are symmetric about their centreline, it is only necessary to include half of a crescent width in the computational domain. Following Longuet-Higgins & Cokelet (1978) and Xue *et al.* (2001), we present results in the form of a growth curve, where a root-mean-square growth rate $R(t)$ is defined as

$$R(t) = \left[ \frac{\int\int \eta'(x, y, t)^2 \, \mathrm{d}x \, \mathrm{d}y}{\int\int \eta'(x, y, 0)^2 \, \mathrm{d}x \, \mathrm{d}y} \right]^{1/2} . \tag{4.1}$$

We consider the use of filters with polynomial order two, four, six and eight; having 13, 37, 57 and 81 grid points, respectively (note that the second-order filter has a diamond-shaped stencil, while the others have an octagon-shaped stencil). In all

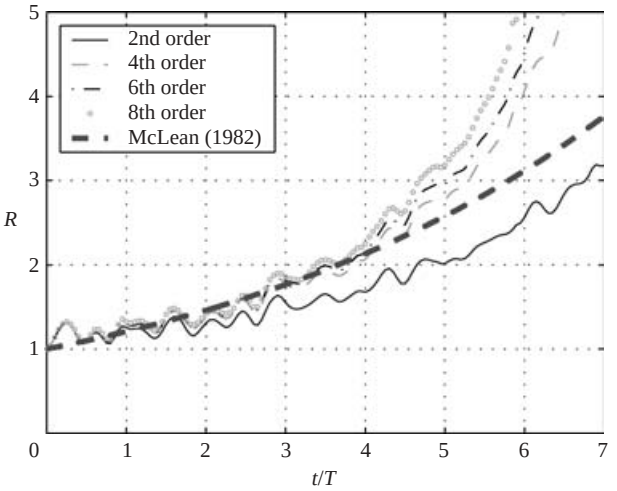


FIGURE 1. Growth rate $R(t)$ of the initial disturbance for simulations using smoothing filters with polynomial order ranging from two to eight. Also shown is the theoretical curve from the linear stability analysis of McLean (1982), given by $\exp(0.0316\sqrt{gk_0}t)$.

simulations, the filter is applied at every time step. Fourier analysis of the various filters has shown that the higher-order smoothing filters (order greater than two) have a much less pronounced effect on high-frequency modes (discretized roughly with 10 or fewer grid points per wavelength), thus they provide the cleanest evolution based solely on the system of nonlinear PDEs. For each test, a domain covering half a crescent width in $y$ (17 grid points) and two full incident wavelengths in $x$ (81 grid points) is used for the determination of $R(t)$, starting at $x = 7L$. Values for $\eta'$ are obtained by subtracting the computed values for $\eta$ in each simulation from those for a similar simulation using unperturbed streamfunction incident waves.

The resulting growth curves are presented in figure 1 for the first $7T$, as is the theoretical curve based on the linear stability analysis of McLean (1982). Xue *et al.* (2001) present a similar growth curve from a simulation with the same nonlinearity and $\epsilon$ using a second-order 13-point filter (applied intermittently), which matches the theoretical curve very well. Figure 1 confirms their finding, demonstrating an excellent match for the first $4T$. Deviations occur at later stages of growth, however. A comparison of the various smoothing filters clearly shows that the second-order smoothing filter hampers the long-term growth of the instability. This can be remedied to some degree by applying the filter intermittently, e.g. at every other time step, however, our experience has shown that the use of higher-order filters results in less interference. As demonstrated by the simulations with the higher-order filters, when the fully nonlinear evolution of these patterns is *uninhibited* (or nearly so), we obtain an accelerated growth rate for $t \geqslant 4T$, which significantly exceeds that predicted by the linear analysis. There is no fundamental reason to expect the fully nonlinear growth to follow precisely the theoretical linear curve after the onset of the instability, as the growth itself is due to nonlinear interactions. The sudden appearance of these patterns as described in physical experiments supports this contention. Such an acceleration is even stated in Su *et al.* (1982), though it is doubtful that this observation is based on any quantitative information. Based on our results, we consider such an acceleration of the growth likely in the fully nonlinear evolution of these patterns. The results of all the filters with polynomial order four or higher are reasonably similar, and have a

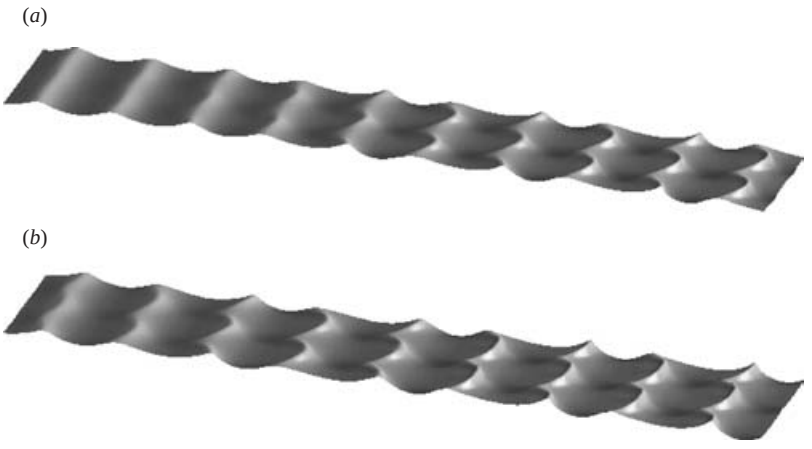


FIGURE 2. Computed free surfaces (to scale) for L2 crescent waves with $H/L = 0.105$ for (*a*) $\epsilon = 0.05$ at $t = 11.45T$, and (*b*) $\epsilon = 0.16$ at $t = 7.45T$.

much less pronounced influence on the growth rate than does the second-order filter. We therefore adopt the fourth-order filter for the remainder of this section, unless otherwise noted. A more complete investigation of the physical processes can be found in § 4.5, where we investigate the growth into a developed crescent wave field.

### 4.3. *Characteristics of the L2 crescent patterns*

In this section, the characteristics of the phase-locked L2 crescent pattern are investigated. All results again use $H/L = 0.105$ with the fourth-order smoothing filter applied at every time step. Figure 2 shows computed surface elevations from simulations using $\epsilon = 0.05$ and 0.16 near their final state (i.e. $t = 11.45T$ and $7.45T$, respectively). Multiple widths of the computed free surface are obtained throughout simply by repeatedly reflecting the results over the $y$-axis. The perturbed incident waves develop very rapidly into crescent-shaped patterns, particularly with $\epsilon = 0.16$. The main effect of smaller $\epsilon$ is simply to slow the crescent growth (similar findings are discussed in Xue *et al.* 2001). Other differences are also apparent, however. Notably, the crescents with $\epsilon = 0.16$ develop a much flatter face than do those with $\epsilon = 0.05$. Slightly after the states shown in figure 2, the waves become extremely steep, and the simulations break down, almost certainly because of wave breaking. This process is consistent with the observations of Su *et al.* (1982), who repeatedly refer to the crescent patterns as 'spilling breakers'. Throughout this work these computational breakdowns are characterized by a significant increase in the number of iterations required for solutions of $\boldsymbol{Ax} = \boldsymbol{b}$, and simulations are stopped after 200 iterations are reached without convergence. Figure 3 also shows a smaller portion of the final L2 pattern in more detail for the case with $\epsilon = 0.05$. From these figures, many of the distinguishable features described by Su *et al.* (1982) and Su (1982) can be seen clearly. The waves have noticeable front–back asymmetry – with the steepest part of the wave occurring on the front face, the crests are shifted by half the width of the crescents on successive rows (i.e. the L2 pattern), deep troughs appear in front of the crescent face, and flattened troughs are evident directly behind the crests.

Figure 4 shows contour plots at two locations from the simulation with $\epsilon = 0.16$. The flattened troughs behind each crescent, and the deep troughs in front of each crescent face are again very apparent. Figure 4(*a*) demonstrates some additional features – namely a steepening of the crescent 'shoulders', and a rising 'delta' region

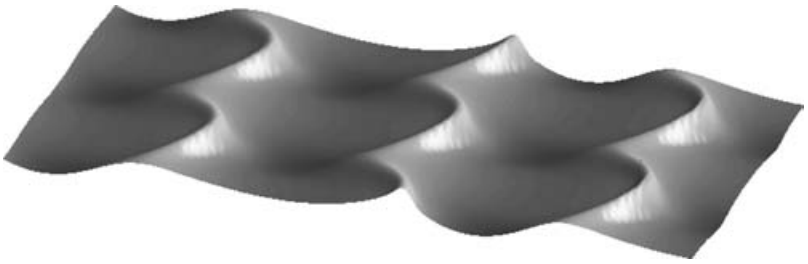

FIGURE 3. Computed free surface (to scale) for L2 crescent waves with $H/L = 0.105$ and $\epsilon = 0.05$ at $t = 11.45T$.

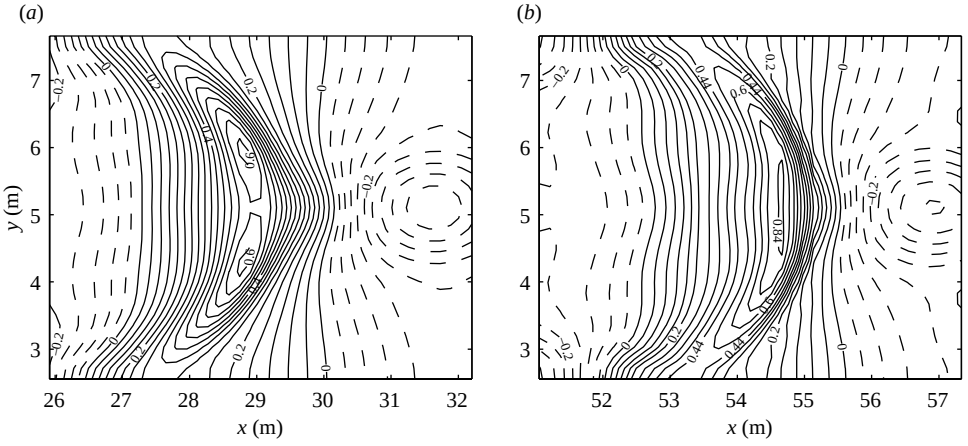


FIGURE 4. Contour plots from simulations with $H/L = 0.105$ and $\epsilon = 0.16$ at $t = 7.45T$ beginning at (*a*) $x = 4.125L$ and (*b*) $x = 8.125L$. Note that in (*b*) the contour interval varies for $\eta > 0.2$ m (it is constant between each labelled contour).

in front of the crescent face. Similar features were also observed in the simulations of Xue *et al.* (2001), just prior to breaking, and this figure compares qualitatively quite well with their figure 12. These features have disappeared in the state shown in figure 4(*b*), however, with the steepest part of the wave occurring along the crescent centre. This is consistent with the description of Su *et al.* (1982), who clearly report spilling breakers over the front (central) face of the wave. Contour plots from the simulation with $\epsilon = 0.05$ are similar to figure 4(*b*), again having a less flattened face, with the steepest part of the wave at the centre.

Having established that the model results are qualitatively similar to those observed in physical experiments and in previous computations, we now attempt to validate the model in a more quantitative manner. As noted in Shrira *et al.* (1996), despite their seemingly common character and easiness of observation, quantitative experimental information available for such patterns is rather meager. Su (1982), however, does give some characteristic ratios for a typical L2 crescent wave generated using an incident wave of this nonlinearity. Note that there is seemingly a mistake in the definition for $h_{12}$ in Su (1982, figure 12). We adopt the measures used in Su *et al.* (1982) and Xue *et al.* (2001) for comparison here, which are shown in figure 5(*a*) along $y = L_y/2$. Also shown in figure 5(*b*) is the free surface along $y = L_y/4$, which is qualitatively similar in form to a plane Stokes wave and compares well with similar plots in Su (1982) and Xue *et al.* (2001).

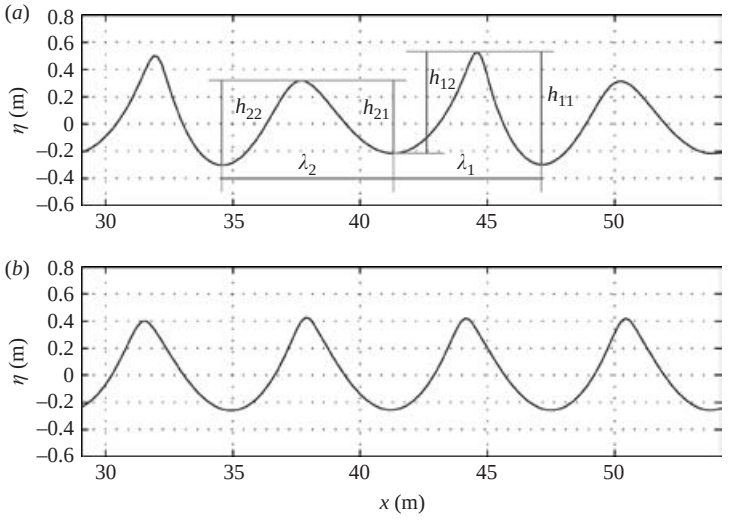


FIGURE 5. Computed free surface elevations at $t = 10T$ with $H/L = 0.105$ and $\epsilon = 0.05$ along ($a$) the crescent centreline $y = L_y/2$ and ($b$) $y = L_y/4$.

| | | $\epsilon = 0.05$ | | | | $\epsilon = 0.16$ | | | |
|---|---|---|---|---|---|---|---|---|---|
| | Su (1982) | $t/T = 8$ | 9 | 10 | 11 | 4 | 5 | 6 | 7 |
| $\lambda_2/\lambda_1$ | 1.28 | 1.16 | 1.16 | 1.22 | 1.29 | 1.22 | 1.26 | 1.16 | 1.22 |
| $h_{11}/h_{12}$ | 1.10 | 1.11 | 1.11 | 1.18 | 1.19 | 1.13 | 1.23 | 1.15 | 1.30 |
| $h_{21}/h_{22}$ | 0.88 | 0.89 | 0.86 | 0.78 | 0.74 | 0.86 | 0.77 | 0.81 | 0.67 |
| $h_{11}/h_{21}$ | 1.66 | 1.36 | 1.55 | 1.80 | 2.05 | 1.44 | 1.62 | 1.79 | 2.11 |
| $s_{max}$ | 0.65, 1.02 | 0.51 | 0.66 | 0.79 | 1.42 | 0.62 | 0.59 | 0.83 | 0.92 |

TABLE 2. Characteristic ratios for measured and computed phase-locked L2 crescent wave patterns with $H/L = 0.105$ (at full-period intervals).

Table 2 gives a quantitative comparison of the characteristic ratios from figure 5($a$) with those reported in Su (1982) for both simulations, i.e. with $\epsilon = 0.05$ and 0.16. As we have shown, our simulations result in continually developing patterns, thus measurements are taken at full-period intervals for comparison. As can be seen in table 2, the results from both simulations compare well with the experimental measurements. The computed results are similar in quality to those obtained from the boundary-element model of Xue *et al.* (2001). Notable exceptions are the results for $\lambda_2/\lambda_1$, which match the experiments better than those of Xue *et al.* (2001), who attributed this to possible lower accuracy in the measurements (another possible explanation is their use of periodic boundaries in $x$, which do not allow for free adjustment of the lengths in this direction). The computed results for the maximum slope of the water surface $s_{max}$ (calculated here using a centred second-order finite-difference approximation) initially match well with the first (lower) value of $s_{max} = 0.65$ given by Su (1982) (as well as those obtained in Xue *et al.* 2001). As the simulations progress, the waves steepen significantly, and surface slopes closer to the second (and significantly higher) reported value of $s_{max} = 1.02$ are obtained. A precise indication of where breaking occurs is beyond the capabilities of the present model, though we speculate that it roughly corresponds to the point of computational breakdown. In

general, the computed results are acceptable, and give confidence that the Boussinesq model is capable of reproducing this deep-water highly nonlinear phenomenon accurately.

### 4.4. *The effects of nonlinearity*

We will now use the model to demonstrate the effects of variable nonlinearity on the general features of the phase-locked L2 class of crescent pattern. We consider cases with $H/L = 0.096$, 0.111, 0.127 and 0.131. The simulation with $H/L = 0.096$ uses $\epsilon = 0.16$, whereas the others use $\epsilon = 0.05$. Each simulation uses the spatial and temporal discretizations from table 1, again corresponding to the most unstable transversal class II mode for each nonlinearity according to McLean (1982). Such a demonstration is demanding given the high wave steepness of even the incident carrier waves, and a model with excellent nonlinear characteristics in deep water is essential for this task.

Figure 6 shows computed free-surface elevations near the end of each simulation (with the exception of the case with $H/L = 0.096$, owing to severe steepening of the wave fronts). We mention that this point is reached very quickly with simulations having $H/L = 0.127$ and 0.131, after $4.2T$ and $3.95T$, respectively. The results with $H/L = 0.096$ are noticeably less defined than the others, presumably because of the relative weakness of the instability at this nonlinearity. The rising crescent shoulders noted in § 4.3 are again apparent in this simulation. The results with $H/L = 0.111$ are similar to the results in figure 3 (with $H/L = 0.105$). As the nonlinearity is further increased, the dominant instability significantly increases its length in the $y$-direction (as predicted by McLean 1982, and indicated in table 1), resulting in much wider patterns with less pronounced crescent tails, as can be seen in figures 6($c$) and 6($d$). The deepened trough regions in front of the crescent faces are also nearly absent in these patterns. This may simply be due to a lack of overall development before computational breakdown, however.

### 4.5. *Discussion of physical processes*

To provide an indication of the physical processes involved in the phase-locked L2 crescent patterns, computed Fourier amplitudes from the simulation with $H/L = 0.096$ and $\epsilon = 0.16$ are shown in figure 7. As pointed out by McLean (1982), the three-dimensional class II instability does not become dominant until $H/L \approx 0.10$. However, the nonlinearity used here is close enough to this value to be physically relevant. Moreover, this simulation is useful, as it does not result in a computational breakdown within the model domain. Hence, enough data is available to perform an accurate time series analysis, providing insight into the dominant physical processes involved. The current simulation is stopped after 5000 time steps (i.e. $125T$). As seen in figure 7, in addition to the primary wave and its higher (bound) harmonics ($\omega/\omega_0 = 1, 2, 3$), the figure shows very clear spikes at $\omega/\omega_0 = 0.5$, 1.5, 2.5 and 3.5, with the amplitude at $\omega = 1.5\omega_0$ being by far the largest. This provides very strong evidence that the dominant physical process for the modelled L2 crescent patterns is indeed the established quintet resonant condition identified in Shrira *et al.* (1996). This condition satisfies

$$\boldsymbol{k}_1 + \boldsymbol{k}_2 = 3\boldsymbol{k}_0, \quad \omega_1' + \omega_2' = 3\omega_0, \tag{4.2}$$

where $\boldsymbol{k}_0 = \langle k_0, 0 \rangle$. In the general L2 case, this corresponds to a symmetric pair of satellites, i.e. $\boldsymbol{k}_1 = \langle 1.5k_0, k_y \rangle$ and $\boldsymbol{k}_2 = \langle 1.5k_0, -k_y \rangle$, with $\omega_1' = \omega_2' = 1.5\omega_0$. Additional triad interactions between the primary wave and the $\omega = 1.5\omega_0$ and $2.5\omega_0$ harmonics, as well as with the $\omega = 2.5\omega_0$ and $3.5\omega_0$ harmonics are also apparent. These

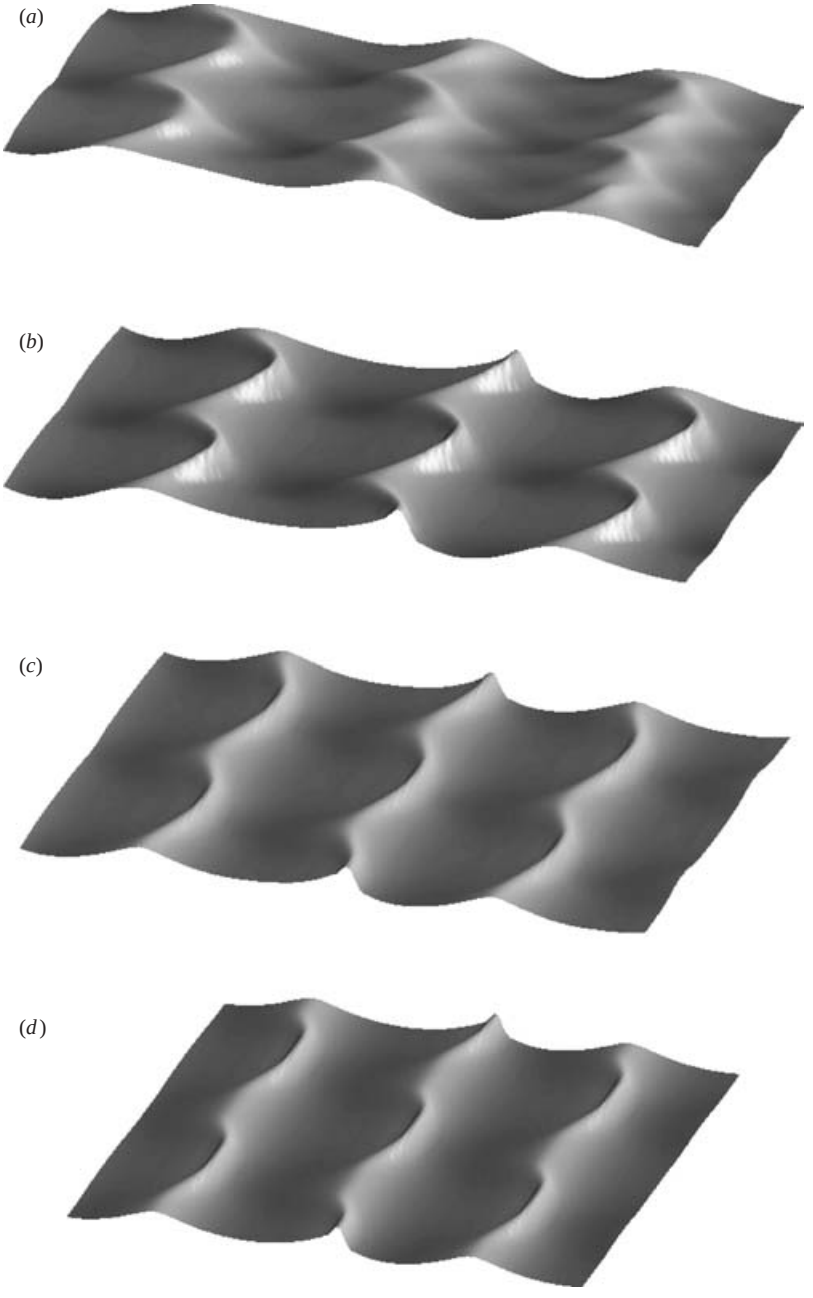


FIGURE 6. Computed free surfaces (to scale) for phase-locked L2 crescent wave patterns with (*a*) $H/L = 0.096$, $t = 50T$; (*b*) $H/L = 0.111$, $t = 8.7T$; (*c*) $H/L = 0.127$, $t = 4.2T$; and (*d*) $H/L = 0.131$, $t = 3.95T$.

interactions are of secondary importance, however, they probably become more significant as the evolution progresses and the waves steepen. Figure 7 compares particularly well with the spectrum given in Collard & Caulliez (1999) (also those from Su 1982) for an experimentally observed L2 pattern, giving further confidence in the Boussinesq model. Fourier amplitudes from other $x$-locations have been found

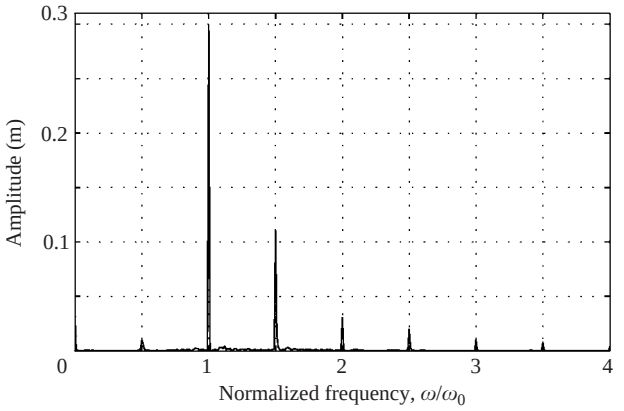


FIGURE 7. Computed Fourier amplitudes from an L2 crescent wave simulation ($H/L = 0.096$, $\epsilon = 0.16$) from a time series at $\langle x, y\rangle = \langle 5L, L_y/2\rangle$ using time steps 1001–5001.

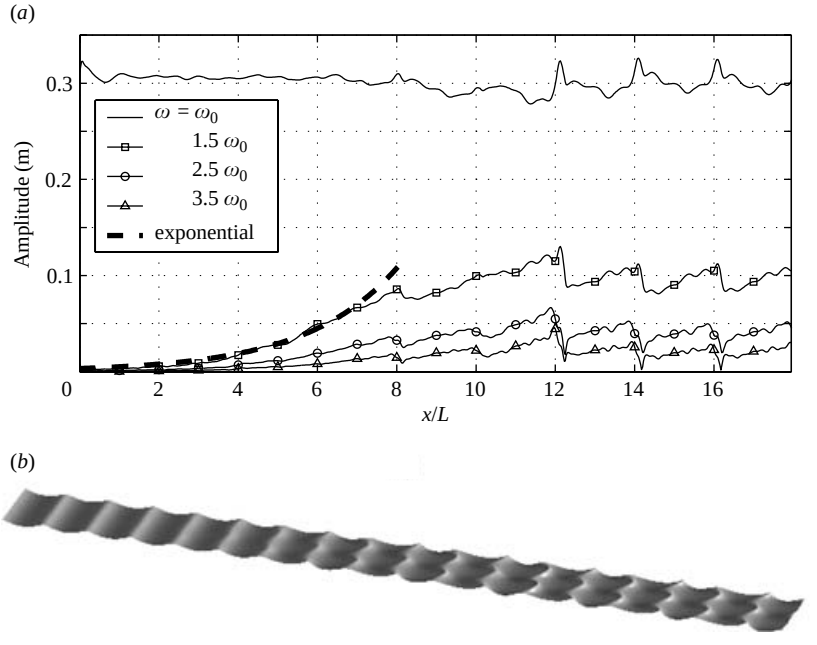


FIGURE 8. Computed (*a*) harmonic amplitudes and (*b*) free surface (to scale) at $t = 17.95T$ from an L2 crescent wave simulation with $H/L = 0.105$ and $\epsilon = 0.01$. The exponential curve in (*a*) is given by $(\epsilon H/2)\exp(2.3 \cdot 0.0316\sqrt{gk_0}(x/c))$.

to be very similar. Also noteworthy is the relative insignificance of the $\omega = 0.5\omega_0$ subharmonic. This is consistent with triad interactions in deep water for which the subharmonic energy transfer is less than the superharmonic transfer.

To gain further insight, figure 8 shows computed harmonic amplitudes and the free surface at the end state from a simulation using $H/L = 0.105$ and $\epsilon = 0.01$ on a $1025 \times 17$ computational grid, again with the fourth-order smoothing filter. The small value for $\epsilon$ probably provides a development more in line with a truly infinitesimal disturbance. This simulation lasts for $17.95T$, and the harmonic analysis uses a

linear-least-squares fit from data covering the final $2T$ to give an indication of the final evolved state. We stress that by analysing the evolution at the end of the simulation rather than at the beginning (as was in part done in §4.2), we are now demonstrating the nonlinear growth into an existing wave field.

In figure 8($a$), an initial exponential growth along the channel for each of the higher harmonics is clearly demonstrated for $0 < x < 7L$. The close match with the exponential curve for the $\omega = 1.5\omega_0$ harmonic suggests a fully nonlinear growth rate near the end of the simulation of roughly 2.3 times larger than that predicted by the linear analysis of McLean (1982). This is consistent with the accelerated growth at the later stages in figure 1. The stability analysis corresponds specifically to infinitesimal perturbations of a plane progressive wave train, thus the deviation presented here (involving progression into a developed wave field) may not be altogether surprising. The development in these circumstances is equally important, however, as it corresponds to the state most often observed in wave tank experiments. Note that the computed growth rate of the $\omega = 1.5\omega_0$ harmonic, e.g. at $x = 1.6L$, is $0.0356\sqrt{gk_0}$, thus we can still confirm growth rates near the inception similar to the theoretical value of $0.0316\sqrt{gk_0}$ (see table 3). Similar harmonic analyses using data from earlier time spans have shown that the $\omega = 1.5\omega_0$ harmonic gradually climbs the exponential curve along $x$ at a rate approximately equal to the deep-water group velocity $c_g = c/2$, i.e. roughly matching the curve up to $x = c_g t$ as time progresses. The strength of the harmonic effectively levels downstream of this location. For example, in the present simulation, this suggests a deviation from the exponential curve at the end state at $x \approx c_g 17.95T \approx 9L$. As mentioned, the deviation in figure 8 begins at $x \approx 7L$, the difference being precisely the equivalent length of the time span used in the harmonic analysis. Just after the point shown in figure 8($b$) the wavefront at $x \approx 12L$ steepens, and the simulation breaks down.

Figure 8 also provides an insight into the harmonic composition of the crescent waves at various stages in their development. In figure 8($b$), crescent patterns have clearly emerged at $x \approx 7L$, but they are not so well defined. For $7L < x < 12L$, the higher harmonics maintain a slowed evolution, sharpening the characteristics of the crescent patterns. From figure 8($a$), the fully nonlinear physical process is again seen to be a complicated combination of resonant quintet interactions, with quadratic nonlinearities forcing additional $\omega = 2.5\omega_0$ and $3.5\omega_0$ harmonics. The basic quintet interaction results in the characteristic crescent patterns, while the higher harmonics add definition to the observed forms. Computed Fourier amplitudes from a space series of free-surface elevations are also shown in figure 9 along $y = L_y/2$. Spikes are again apparent at $k = 1.5k_0$, $2.5k_0$ and $3.5k_0$, clearly indicating that each of the higher harmonics is bound to the carrier wave (i.e. each having the same celerity $\omega/k_x = \omega_0/k_0$).

We finally remark that there is some contention in the literature on the role of dissipation in the formation of crescent wave patterns. Shrira *et al.* (1996) concluded that, within the framework of their Hamiltonian system, it is not possible to explain the emergence of any long-lived three-dimensional patterns. In a reappraisal of their system, however, Craig (2001) found that three-dimensional crescent-shaped waves indeed occur, and that these solutions are of permanent form, without the presence of breaking or other mechanisms of dissipation. Xue *et al.* (2001) also argue that crescent patterns arise naturally from nonlinear wave evolutions, which in our view seems logical given that they are initiated by the class II instability (which assumes no dissipation). In the present numerical study (as well as in Xue *et al.* 2001), we do add light numerical smoothing to prolong our simulations in these highly nonlinear

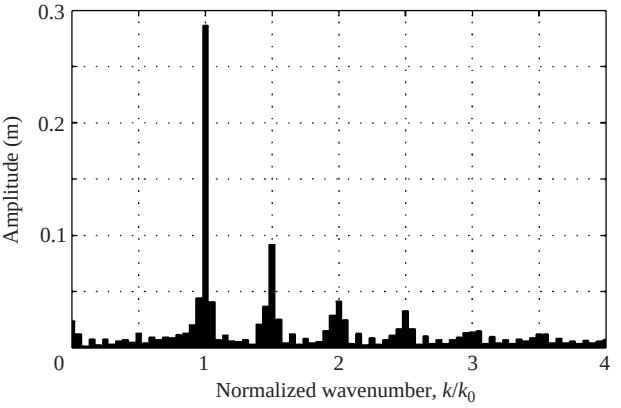


FIGURE 9. Computed Fourier amplitudes from an L2 crescent wave simulation with $H/L = 0.105$, and $\epsilon = 0.01$ from a space series at $t = 17.95T$, along $y = L_y/2$. The analysis uses grid points 126–925.

circumstances, therefore, one may argue that we can hardly discriminate between conservative and dissipative cases. We have, however, also made simulations without smoothing, which lead to essentially similar crescent patterns (albeit noisy and less developed). Hence, we are convinced that the smoothing plays a relatively minor role in the developments presented here (in line with § 4.2), and agree with Xue *et al.* (2001) and Craig (2001) that crescent waves can indeed develop without dissipation. In none of our simulations do they take a permanent form, however. The present model suggests a complicated evolution of the crescent waves, consisting of three distinct periods: (i) An initial linear growth (initiated by the class II instability), (ii) an accelerated nonlinear growth fuelled by resonant quintet interactions, and (iii) a breaking stage. Thus, we feel it is probably the dissipation due to breaking that ultimately counteracts the unstable growth, resulting in waves of relatively constant form as observed, for example, in Su *et al.* (1982).

## 5. Oscillating crescent patterns

Having examined the phase-locked crescent wave patterns, we now turn our attention to those with an oscillating nature – where well-defined crescents no longer propagate in a quasi-steady form, but emerge and disappear repeatedly, shifting by a half-width in the $y$-direction with each successive emergence. Such oscillating patterns have been recently observed in a wave tank in a very pure form by Collard & Caulliez (1999). Deviations from the 'standard' L2 pattern were also reported in the experiments of Melville (1982), as well as in Su *et al.* (1982) and Su (1982) (i.e. the L3 and L4 patterns). In this section we investigate the long-term evolution of crescent waveforms initiated by a double perturbation. All simulations in this section use a $513 \times 17$ computational grid.

### 5.1. *Transition from* $\langle k_{x1}, k_{x2}\rangle = \langle 4/3, 5/3\rangle k_0$ *to* $\langle 1, 2\rangle k_0$

For the generation of oscillating crescent waves, we first consider a simulation using a double perturbation (both as described in § 3), with $k_{x1} = 4k_0/3$, $k_{x2} = 5k_0/3$, and $k_{y1} = k_{y2} = 1.32k_0$, superimposed over streamfunction incident waves with $H/L = 0.096$. Such a perturbation initially excites quintet resonant interactions involving the primary wave and two sets of unsymmetric satellites. Recall that the

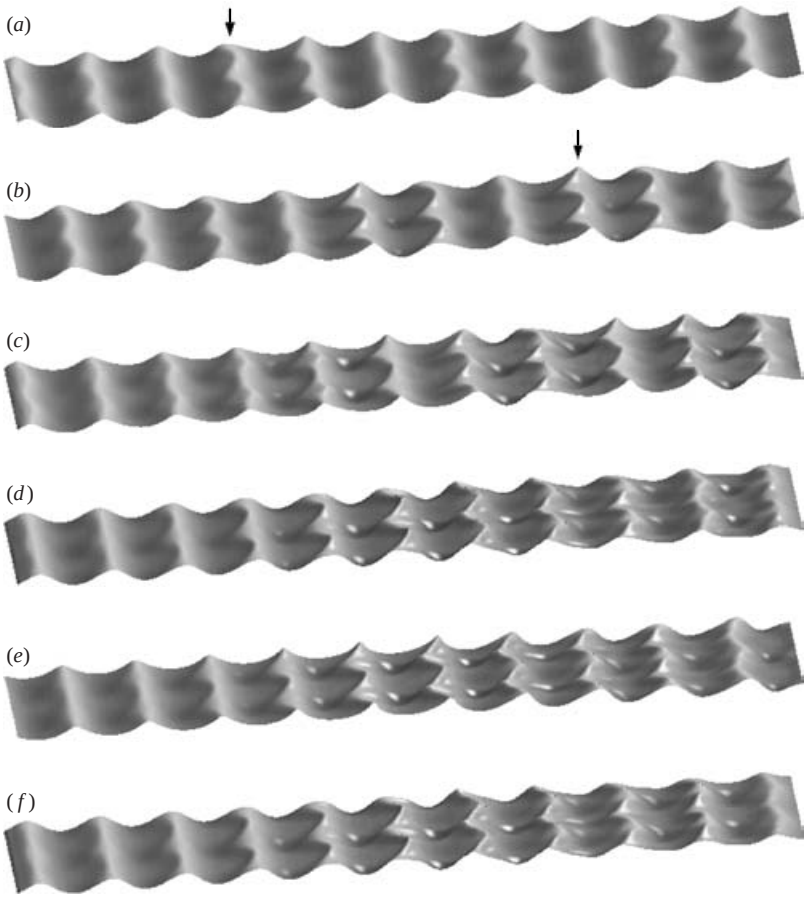


FIGURE 10. Evolution of oscillating crescent waves (transitioning from $\langle k_{x1}, k_{x2}\rangle = \langle 4/3, 5/3\rangle k_0$ to $\langle 1, 2\rangle k_0$) at (*a*) $t = 4.1T$, (*b*) $t = 8.8T$, (*c*) $t = 14.2T$, (*d*) $t = 30.3T$, (*e*) $t = 31.8T$ and (*f*) $t = 33.3T$. The vertical scale is multiplied by two.

perturbation in § 3 is equivalent to the superposition of two travelling components with $\pm k_y$, thus two sets of resonant conditions are indeed satisfied. For both perturbations $\epsilon = 0.08$ is used, and the corresponding frequencies are defined according to (3.6), i.e. $\omega_1' = 4\omega_0/3$ and $\omega_2' = 5\omega_0/3$, which again assumes bound perturbations. The perturbation wavenumbers define the initial conditions throughout the computational domain, while the frequency perturbations are only imposed at the wavemaker. Thus, if the two do not satisfy a naturally occurring quintet resonant interaction we can expect a transition to occur. We wish to investigate the long-term nature of this generation, thus we use an extended simulation run for 5000 time steps (i.e. $125T$). The fourth-order smoothing filter is again applied at each time step.

Computed free surfaces are shown in figure 10 at six instants, which give a good indication of the overall model development. Consistent with the observations from a reasonably similar simulation in Xue *et al.* (2001) (lasting for slightly more than $4T$), our simulations indicate that, unlike the L2 case (with $k_x = 1.5k_0$), the initial patterns are no longer bound to the carrier waves. Rather, the individual crescents oscillate. Figures 10(*a*) and 10(*b*) show typical free surfaces early in the simulation (at $t = 4.1T$ and $8.8T$, respectively), which compare reasonably well to figure 19 in Xue *et al.*

(2001). Note that, at this point in the simulation, the pattern at the downstream end of the domain is repeated every $3L$, as specified by the initial conditions with $\langle k_{x1}, k_{x2}\rangle = \langle 4/3, 5/3\rangle k_0$. By following the marked carrier wave from figure 10(*a*) to 10(*b*), it is seen that half a complete oscillation cycle takes roughly $4.7T$, implying a full oscillation period of $T^* \approx 9.4T$. An explanation of the wavenumber and frequency combinations involved in the oscillating patterns is provided at the end of the current section.

Figure 10(*c*) shows a slightly more evolved state (at $t = 14.2T$), where the model is in a transitional period, i.e. the pattern generated from the initial conditions is indeed transitioning to one forced from the frequency disturbance at the wavemaker. Near the wavemaker region in figure 10(*c*), the crescent patterns are repeated roughly every carrier wavelength, and are beginning to oscillate in phase with one another. Near the end of the domain, a distinct L3 pattern having the high–high–low (HHL) structure reported in Su *et al.* (1982) and Su (1982) is apparent. This is the first clear computation of such a pattern to the authors' knowledge. We stress that this formation occurs momentarily, and does not progress as a constant form.

As time evolves further, the initial conditions become washed out of the computational domain, and the structured oscillations prevail throughout the computational region, as shown in figure 10(*d*). At this point, the resulting patterns are strikingly similar to the recently observed oscillating crescent patterns of Collard & Caulliez (1999), which have a similar arrangement, and are reported to oscillate with a period of $T^* \approx 3T$. This resemblance could in fact be expected, as the perturbation frequencies at the wavemaker are reasonably close to the measured values from Collard & Caulliez (1999) of $1.36\omega_0$ and $1.64\omega_0$. Computed free surfaces are shown again $1.5T$ later during the next clear instance of crescent formation in figure 10(*e*). Here, the crescents have shifted by half a crescent width in the $y$-direction from the formation in figure 10(*d*), in agreement with the description of Collard & Caulliez. Finally, figure 10(*f*) shows the computed free surface after another $1.5T$, where the crescents have shifted back to their original position shown in figure 10(*d*). This type of oscillating pattern prevails for the remainder of the simulation. A complete oscillation cycle as seen from figures 10(*d*) to 10(*e*) to 10(*f*) is indeed $T^* \approx 3T$ – in excellent agreement with the physical experiments.

Each crescent in the oscillating formation follows a complicated modulation pattern, which has not been previously detailed. In an attempt to fill this gap, the modulation of a single crescent wave is provided in figure 11, beginning at $x = 5.25L$ and $t = 33T$. Now, the initial conditions are completely washed out of the computational domain, and the model is clearly in a repeating state of dynamic equilibrium. Figure 11(*a*) begins just after the formation of a newly developed crescent, having peaks at $y = 0$, $L_y$, and $2L_y$. Notably, at this point in the evolution – where the crescent is near its most developed state – the deepened trough regions in front of and behind the crests are nearly absent. The waves pass through this state, very quickly, providing a good means for a more precise estimation of the oscillation period. Soon after this state, the crescent tails rise slightly and the crests begin to flatten, as shown in figure 11(*b*). Note that here, deepened troughs are beginning to emerge following the crescent tails. The crests continue to flatten, until becoming nearly level, as shown in figure 11(*c*). At roughly this point, the troughs following the crescent tails are at their most defined state. The crests continue to flatten until becoming nearly straight, as shown in figure 11(*d*). The tails then begin to push forward, fuelling small spikes emerging from the wave crests, as shown in figure 11(*e*). The tails continue their collapse and the spikes enlarge, eventually forming entirely new crescents, as seen in figure 11(*f*). The trough

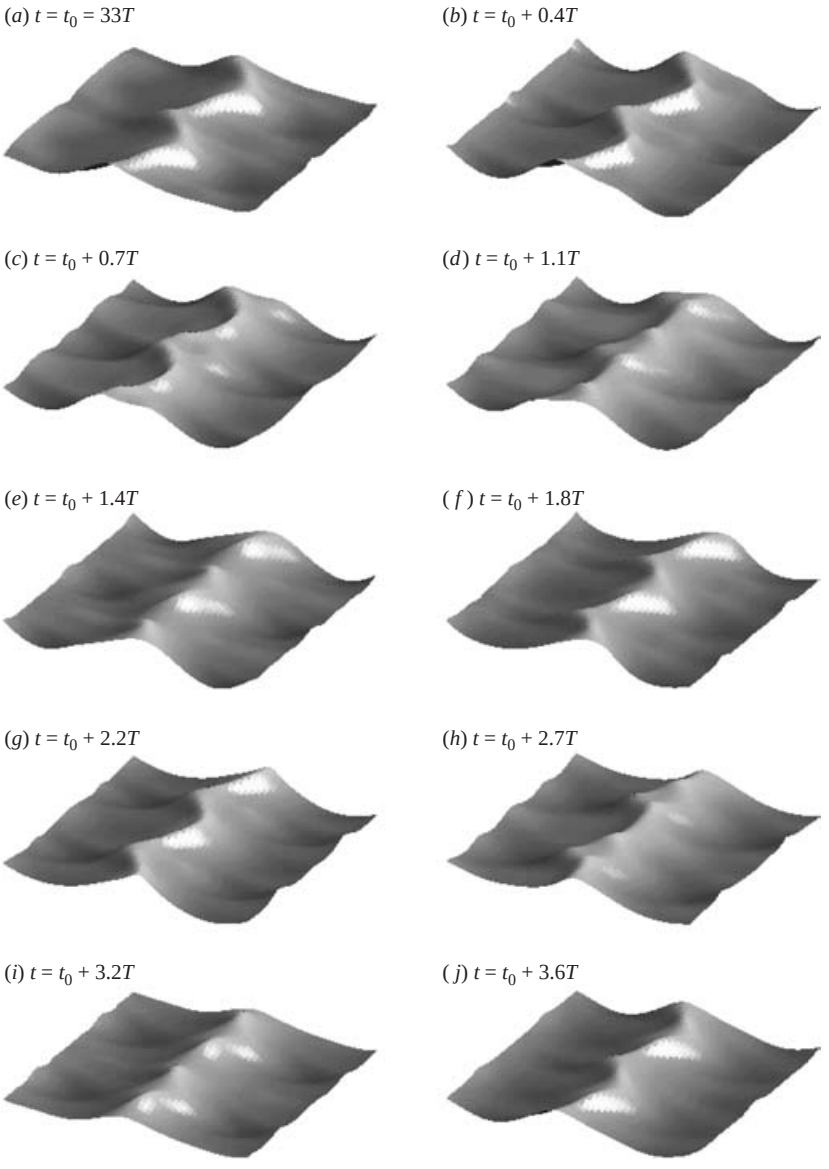


FIGURE 11. The evolution of an oscillating crescent wave starting at $t_0 = 33T$ and $x = 5.25L$. The vertical scale is multiplied by one and a half.

regions following the crescent tails are again nearly absent in this figure, as was the case in figure 11($a$). Note also that the crescent forms in figure 11($f$) have shifted half a crescent width in the $y$-direction from the initial form seen in figure 11($a$).

From the point shown in figure 11($f$), the waves follow a similar process, eventually arriving back at a state resembling that shown in figure 11($a$). This can be seen in the evolution from figure 11($f$) to 11($j$). From figure 11, this particular cycle, in fact, takes slightly longer than the previously mentioned $3T$. Our results indicate that this figure is closer to $3.6T$, though estimates vary slightly depending on the precise measurement location. Specifically, estimates ranging from $T^* = 3.1T$ near the left-hand side of the computational domain to the illustrated $3.6T$ near the right-hand

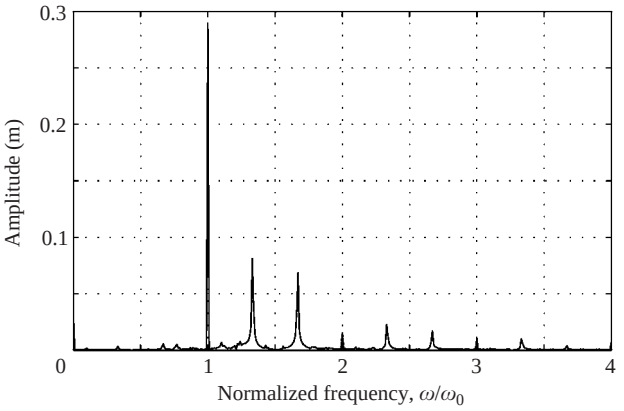


FIGURE 12. Computed Fourier amplitudes based on a time series from the oscillating crescent simulation from § 5.1 at $\langle x, y\rangle = \langle 8L, L_y/2\rangle$. The analysis uses time steps 1001–5001.

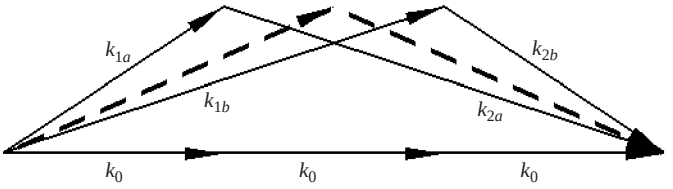


FIGURE 13. Resonant wavevector quintets for the phase-locked L2 (dashed) and the oscillating crescent (solid) patterns. A similar figure can be found in Collard & Caulliez (1999).

side have been measured (the latter is shown, as these are the most defined). These are still similar to the estimated $3T$ of Collard & Caulliez (1999) (note also that they do not specify a value for $H/L$).

To gain knowledge of the physical processes involved in the modelled oscillating crescent wave patterns, computed Fourier amplitudes from a time series taken at $\langle x, y\rangle = \langle 8L, L_y/2\rangle$ are shown in figure 12. The analysis uses time steps 1001–5001, when the initial conditions are completely washed out of the computational domain. Plots from other $x$-positions have been found to be qualitatively similar. After the primary wave, two significant spikes can be observed in the spectrum at $\omega = 1.33\omega_0$ and $1.67\omega_0$. As expected, these correspond precisely to the frequencies imposed at the wavemaker region. Additional higher harmonics are also clearly present. As the patterns at the end of the simulation are repeated roughly every primary wavelength, the corresponding wavenumbers can be estimated as $k_{x1} \approx k_0$ and $k_{x2} \approx 2k_0$, as discussed by Collard & Caulliez. These are clearly different from the initial conditions. The $y$ wavenumbers can obviously be obtained from the transversal width of the computational domain. This combination clearly satisfies the quintet resonant condition (4.2) with two unsymmetric satellite pairs. This condition is illustrated (for the wavenumbers) in figure 13 for both symmetric and unsymmetric cases. For clarity, the first quintet resonant interaction involves $\boldsymbol{k}_{1a} = \langle k_0, k_y\rangle$ and $\boldsymbol{k}_{2a} = \langle 2k_0, -k_y\rangle$, whereas the second involves $\boldsymbol{k}_{1b} = \langle 2k_0, k_y\rangle$ and $\boldsymbol{k}_{2b} = \langle k_0, -k_y\rangle$. The corresponding frequencies are $\omega'_{1a} = \omega'_{2b} = 4\omega_0/3$ and $\omega'_{1b} = \omega'_{2a} = 5\omega_0/3$.

The relationship between the oscillation period and the combination of satellite frequencies and wavenumbers can be explained using simple linear superposition

arguments. Consider a linear unidirectional carrier wave $\eta = A\cos(\omega_0 t - k_0 x)$ subject to the sinusoidal perturbation $\eta' = a\cos(\omega' t - k_x x - k_y y)$. In a frame of reference moving with the carrier wave, i.e. letting $x = x^* + (\omega_0/k_0)t$ and $y = y^*$ (where $x^*$ and $y^*$ are the coordinates measured from this moving reference frame), the perturbation wave reads

$$\eta' = a\cos\left(\left(\frac{\omega'}{\omega_0} - \frac{k_x}{k_0}\right)\omega_0 t - k_x x^* - k_y y^*\right). \tag{5.1}$$

Hence, the oscillation period can be expressed as

$$\frac{T^*}{T} = \left|\frac{\omega'}{\omega_0} - \frac{k_x}{k_0}\right|^{-1}. \tag{5.2}$$

Using the observed $T^* \approx 9.4T$ (from figures 10($a$) and 10($b$)) in combination with the initial perturbation wavenumbers $k_{x1} = 4k_0/3$ and $k_{x2} = 5k_0/3$ yields estimates for the initial satellite frequencies of $\omega_1' \approx 1.44\omega_0$ and $\omega_2' \approx 1.56\omega_0$. As expected, these are entirely different from those imposed at the wavemaker. Similarly (after the transition), using the observed $T^* \approx 3.1T$ and the known frequencies $\omega_1' = 4\omega_0/3$ and $\omega_2' = 5\omega_0/3$ yields satellite wavenumbers $k_{x1} \approx 1.01k_0$ and $k_{x2} \approx 1.99k_0$, in almost perfect agreement with the previous estimations. These values will be reconfirmed in § 5.3.

### 5.2. *Transition from* $\langle k_{x1}, k_{x2}\rangle = \langle 5/4, 7/4\rangle k_0$ *to* $\langle 3/4, 9/4\rangle k_0$

We now turn our attention to another simulation resulting in oscillating crescent patterns which are not so distinctly arranged. This simulation uses the same model set-up as in § 5.1 (i.e. $H/L = 0.096$, $\epsilon = 0.08$, $k_y = 1.32$), but with $k_{x1} = 5k_0/4$ and $k_{x2} = 7k_0/4$. The perturbation frequencies at the wavemaker are again obtained from (3.6), i.e. $\omega_1' = 5\omega_0/4$ and $\omega_2' = 7\omega_0/4$.

Figure 14 shows six computed free surfaces, which give a good account of the overall development. The evolution of this system is initially similar to that described in § 5.1. Figures 14($a$) and 14($b$) show computed free surfaces relatively early in the simulation. Following the marked carrier wave from figures 14($a$) to 14($b$) reveals an initial half-cycle of roughly $3.1T$, implying an oscillation period of $T^* \approx 6.2T$. From (5.2), this yields initial perturbation frequencies of $\omega_1' = 1.41\omega_0$ and $\omega_2' = 1.59\omega_0$, which will also be confirmed in § 5.3. Figure 14($c$) shows the computed free surface during the transition from the incident cycle to that imposed by the frequency disturbance at the wavemaker. At this instant, a distinct L4 pattern is apparent, having the high–high–low–low (HHLL) structure described by Su *et al.* (1982) and Su (1982). This is the first computation of such a pattern to our knowledge. As the model continues to evolve, the initial conditions become completely washed out of the computational domain, and the patterns again adopt an entirely different oscillation period. Following the marked carrier wave in figures 14($d$) to 10($e$) to 10($f$), a complete oscillation cycle is now seen to be $T^* \approx 2T$. This cycle persists for the remainder of the simulation. Contrary to § 5.1, these oscillating crescent patterns do not become aligned in straight rows.

To demonstrate the physical processes involved in the final evolved patterns shown in figures 14($d$)–14($f$), we first present computed Fourier amplitudes from a time series in figures 15. This figure again clearly shows the presence of those frequencies imposed at the wavemaker region, i.e. $\omega_1' = 5\omega_0/4$ and $\omega_2' = 7\omega_0/4$. The wavenumbers associated with the oscillating process in figures 14($d$)–14($f$) can be estimated

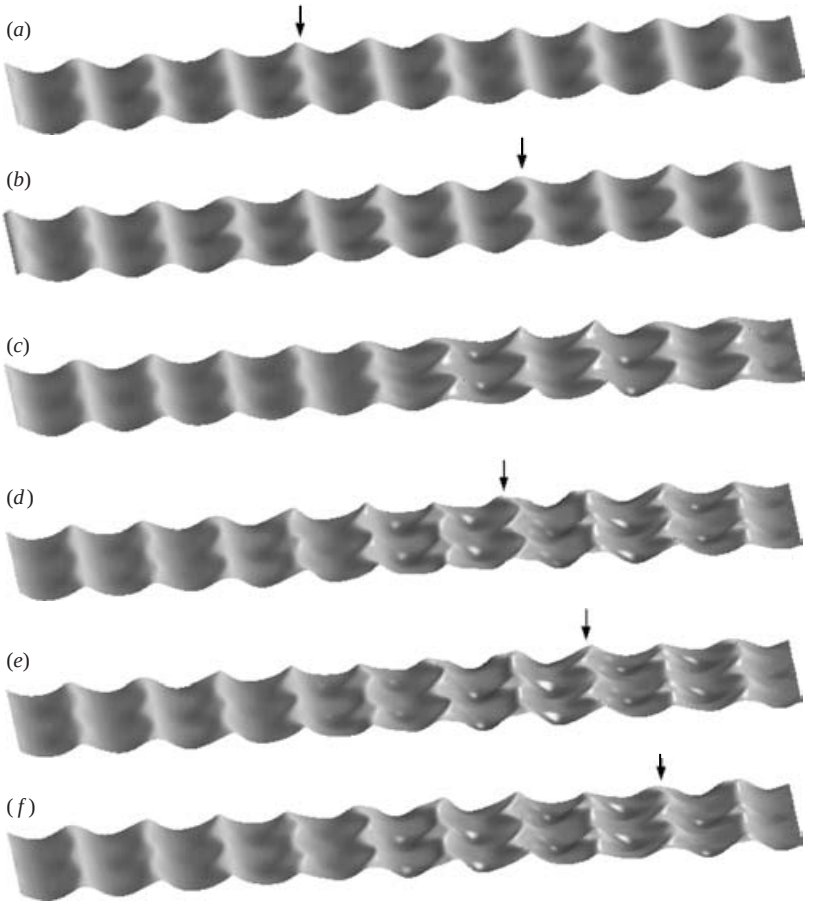


FIGURE 14. Evolution of oscillating crescent waves (transitioning from $\langle k_{x1}, k_{x2}\rangle = \langle 5/4, 7/4\rangle k_0$ to $\langle 3/4, 9/4\rangle k_0$) at (*a*) $t = 3T$, (*b*) $t = 6.1T$, (*c*) $t = 12.2T$, (*d*) $t = 40.9T$, (*e*) $t = 41.9T$ and (*f*) $t = 42.9T$. The vertical scale is multiplied by two.

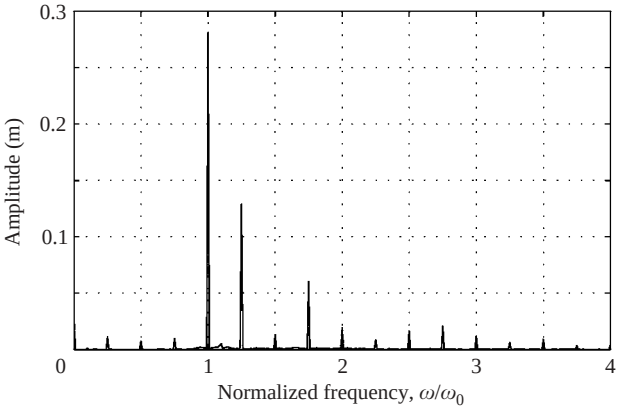


FIGURE 15. Computed Fourier amplitudes from the oscillating crescent wave simulation from § 5.2 from a time series at $\langle x, y\rangle = \langle 7L, L_y/2\rangle$. The analysis uses time steps 1001–5001.

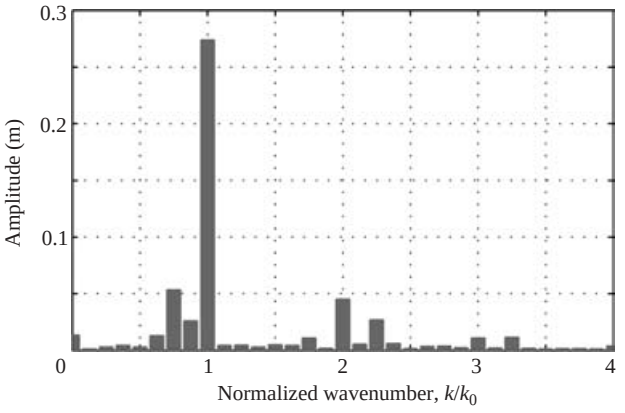


FIGURE 16. Computed Fourier amplitudes from an oscillating crescent wave simulation (as shown in § 5.2, but using a second-order smoothing filter) from a space series at $t = 48T$, $y = L_y/2$. The analysis uses grid points 101–420.

from (5.2) using the known satellite frequencies in combination with the observed $T^* \approx 2T$. This yields $k_{x1} = 3k_0/4$ and $k_{x2} = 9k_0/4$. Computed Fourier amplitudes from a space series along $y = L_y/2$ are shown in figure 16 (from a similar simulation using a second-order smoothing filter). This does not allow for a precise estimation of the wavenumbers, however, it does clearly show spikes at roughly the estimated values, which suffices as confirmation.

This simulation thus illustrates a general oscillating crescent wave pattern, i.e. where the crescents do not become aligned in straight rows as seen in § 5.1. The patterns arranged in straight rows in § 5.1 are merely a special case (visually), owing their aligned nature to the fact that $k_{x1} \approx k_0$, and $k_{x2} \approx 2k_0$.

### 5.3. *A quantitative explanation*

We now pose the question, 'Is it possible to predict the oscillation period given only a set of perturbation wavenumbers satisfying the quintet resonant condition?' Such a method for quantitatively explaining the oscillating crescent waveforms has not been previously presented to our knowledge. The explanation essentially requires a means for estimating the satellite frequencies corresponding to the unstable perturbation wavenumbers, i.e. a dispersion relation of sorts. Note that Collard & Caulliez (1999) use the linear dispersion as a rough estimate. We find that such estimates are indeed very rough, and are not useful in providing accurate quantitative estimations. The required information is embedded in the stability analysis of McLean (1982). Unfortunately, his analysis concentrates primarily on the dominant class II instability (resulting in the phase-locked L2 patterns), giving little quantitative information for those interactions involving unsymmetric satellite pairs.

We therefore undertake a similar analysis, analysing numerically the stability of deep-water carrier waves generated from the streamfunction solution of Fenton (1988) to infinitesimal periodic disturbances resolved on an equidistant spatial grid. To allow for direct comparison with the values of McLean (1982) (who used $g = 1\ \mathrm{m\,s^{-2}}$ and $k_0 = 1\ \mathrm{m^{-1}}$) we present eigenvalues $\sigma$ which are non-dimensionalized with respect to $\sqrt{gk_0}$. The analyses use up to 30 Fourier modes for the streamfunction solution, with the resulting wave discretized with up to 60 equidistant points in space for the corresponding stability analysis. The result is a generalized eigenvalue problem (see McLean 1982, for details). In the present analysis, this is first converted to a standard eigenvalue problem before solving. Specific attention is paid to those

| | Class I | | | | Class II | | | |
|---|---|---|---|---|---|---|---|---|
| $H/L$ | $p$ | $q$ | $\sigma$ | McLean (1982) | $p$ | $q$ | $\sigma$ | McLean (1982) |
| 0.032 | 0.18 | 0 | $-0.088+0.00412$i | $-0.086+0.00409$i | 0.5 | 1.64 | $0+0.00059$i | $0+0.0006$i |
| 0.064 | 0.32 | 0 | $-0.146+0.0134$i | $-0.146+0.0133$i | 0.5 | 1.54 | $0+0.00531$i | $0+0.00523$i |
| 0.095 | 0.47 | 0 | $-0.189+0.0225$i | $-0.189+0.0226$i | 0.5 | 1.33 | $0+0.0210$i | $0+0.0215$i |
| 0.096 | 0.47 | 0 | $-0.188+0.0227$i | — | 0.5 | 1.32 | $0+0.0219$i | — |
| 0.105 | 0.54 | 0 | $-0.204+0.0236$i | — | 0.5 | 1.23 | $0+0.0316$i | — |
| 0.111 | 0.60 | 0 | $-0.215+0.0228$i | $-0.214+0.0227$i | 0.5 | 1.15 | $0+0.0406$i | $0+0.0413$i |
| 0.127 | 0.84 | 0 | $-0.229+0.0119$i | Stable | 0.5 | 0.79 | $0+0.0875$i | $0+0.0888$i |
| 0.131 | 0.90 | 0 | $-0.206+0.0073$i | Stable | 0.5 | 0.65 | $0+0.11$i | $0+0.11$i |
| 0.131 | — | — | — | — | 0.5 | 0 | $0+0.079$i | $0+0.067$i |

TABLE 3. Computed unstable class I and II eigenvalues having maximum imaginary part. Also shown for comparison are those from McLean (1982).

| § | $H/L$ | $p$ | $q$ | $\sigma$ | $T^*/T$ | $\omega_1'/\omega_0$ | $\omega_2'/\omega_0$ |
|---|---|---|---|---|---|---|---|
| 5.1 | 0.096 | 0.667 | 1.32 | $-0.111+0.0213$i | 9.37 | 1.56 | 1.44 |
| 5.1 | 0.096 | 1.0 | 1.32 | $-0.335+0.0171$i | 3.10 | 1.68 | 1.32 |
| 5.2 | 0.096 | 0.75 | 1.32 | $-0.166+0.0205$i | 6.26 | 1.59 | 1.41 |
| 5.2 | 0.096 | 1.25 | 1.32 | $-0.509+0.0117$i | 2.04 | 1.76 | 1.24 |

TABLE 4. Computed unstable class II eigenvalues corresponding to the modelled oscillating crescent wave patterns.

eigenvalues with non-zero imaginary part as these correspond to exponential growth of the unstable modes. The imaginary part determines the growth rate of the initial disturbance, while the real part corresponds to the frequency of the perturbation as seen from a moving frame of reference travelling with the unperturbed wave. A purely imaginary eigenvalue thus indicates an exponentially growing perturbation bound to the carrier wave, as in the general L2 case. Note that in this analysis the perturbation wavenumbers correspond to $\boldsymbol{k}_1 = \langle p+1, q\rangle k_0$ and $\boldsymbol{k}_2 = \langle 1-p, -q\rangle k_0$ for the class I instabilities, and $\boldsymbol{k}_1 = \langle p+1, q\rangle k_0$ and $\boldsymbol{k}_2 = \langle 2-p, -q\rangle k_0$ for the class II instabilities.

Computed eigenvalues for the most unstable class I and II instabilities are shown in table 3, as are those from McLean (1982) for comparison. As can be seen, the two analyses generally compare well with one another, giving confidence in the computed values. In contrast to McLean (1982), however, we detect class I instabilities for $H/L \geqslant 0.127$. This is consistent with the analysis of Kharif & Ramamonjiarisoa (1986, 1990), who found that the class I instability is not stabilized until $H/L > 0.137$. For $H/L < 0.127$, the values shown are converged to at least the three digits shown, while for the higher nonlinearities the convergence becomes somewhat more erratic.

Table 4 shows computed eigenvalues corresponding to the initial and final stages of the two oscillating crescent wave simulations in §§ 5.1 and 5.2. As the real part of $\sigma$ is non-zero in these cases, the corresponding perturbations will no longer be bound as in the L2 case, explaining the oscillatory nature of the patterns. This information can thus be used to provide an estimate for the oscillation period. Recall that the eigenvalues are non-dimensional, and must thus be multiplied by $\sqrt{gk_0}$ to gain physical relevance for the present simulations. The resulting oscillating period can hence be estimated as

$$\frac{T^*}{T_0} = \frac{\omega_0}{\sqrt{gk_0}|\mathrm{Re}\{\sigma\}|}. \tag{5.3}$$

These values are also given in table 4. In each case, the predicted oscillation period matches extremely well with the numerical simulations. In particular, we note that the case with $p = 1.0$ predicts $T^* = 3.10T$, which is very close to the estimation of $3T$ given by Collard & Caulliez (1999). The prediction is also in essentially perfect agreement with the estimate from the model of $3.1T$ occurring nearest to the wavemaker (i.e. before the perturbations reach significant amplitude). The frequencies corresponding to the perturbation wavenumbers can be obtained from

$$\frac{\omega_1'}{\omega_0} = \frac{k_{x1}}{k_0} + \frac{\sqrt{gk_0}\mathrm{Re}\{\sigma\}}{\omega_0}, \quad \frac{\omega_2'}{\omega_0} = \frac{k_{x2}}{k_0} - \frac{\sqrt{gk_0}\mathrm{Re}\{\sigma\}}{\omega_0}. \tag{5.4}$$

These values are also given in table 4. The cases having $H/L = 0.096$ with $p = 1.0$ and $p = 1.25$ result in perturbation frequencies very close to those imposed at the wavemaker regions in §§ 5.1 and 5.2, respectively. The other values (with $p = 0.667$ and 0.75) also confirm the predicted frequencies using (5.2) in §§ 5.1 and 5.2. This analysis has proved to be a very useful means for quantitatively explaining the modelled oscillating crescent wave patterns.

A simulation using $H/L = 0.096$, $k_{x1} = 2k_0$ and $k_{x2} = k_0$ with $\omega_1' = 1.68\omega_0$ and $\omega_2' = 1.32\omega_0$ (as suggested in table 4) results in the development of oscillating crescent patterns aligned in straight rows from the very beginning of the simulation, which then persist indefinitely (within the computational domain). The resulting patterns are essentially the same as those in figures 10(*d*)–10(*f*), thus they are not shown here. This simulation further confirms the accuracy of the stability analysis in quantitatively explaining these oscillating crescent wave patterns.

### 5.4. *On the selection of the Collard & Caulliez (1999) oscillating crescents*

While the previous subsection provides a quantitative explanation of the physics involved in the oscillating crescent wave phenomenon, it does not explain the selection of the specific unsymmetric satellite pair observed in the experiments of Collard & Caulliez (1999), again resulting in the striking alignment of the crescents in straight rows. In the following, we propose that the selection of the observed satellites could in part be an artefact of the tank width, combined with a possible suppression of the class I instability.

Collard & Caulliez (1999) demonstrate their oscillating crescent waves at a carrier frequency $f = 1.3$ Hz ($T = 1/f = 0.769$ s, $\omega_0 = 8.17$ s$^{-1}$) in a tank with depth $h = 0.9$ m and width $w = 2.6$ m. They report an estimated value of $q = |k_y/k_0| = 1.32$, but they do not provide the specific waveheight in the experiment. In an attempt to explain their observations we choose the waveheight of the carrier wave to be $H = 0.0682$ m. A streamfunction solution then yields the wavelength $L = 0.963$ m ($H/L = 0.0708$, $k_0 = 6.52$ m$^{-1}$, $k_0h = 5.87$). Because of the tank width, we will assume that the transversal wavenumbers are limited to the discrete possibilities

$$|k_y| = \frac{\pi n}{w}, \tag{5.5}$$

where $n$ is an integer specifying the number of half transverse wavelengths spanning the width of the tank. Of these, we consider $n = 7$ and 8, giving $|k_y| = 8.46$ m$^{-1}$, $q = |k_y/k_0| = 1.30$, and $|k_y| = 9.67$ m$^{-1}$, $q = |k_y/k_0| = 1.48$, respectively, which are the values closest to the reported $q = 1.32$. Using the stability analysis from § 5.3, setting $\langle p, q\rangle = \langle 1, 1.30\rangle$ does not result in an instability. Alternatively, setting $\langle p, q\rangle = \langle 1, 1.48\rangle$, yields the unstable eigenvalue $\sigma = -0.363 + 0.00587$i, which is, in fact, the dominant class II instability, again provided that $q$ is limited to the discrete values. This results in an oscillating period from (5.3) of $T^* = 2.82T$, and

perturbation frequencies from (5.4) of $\omega_1' = 1.64\omega_0$ and $\omega_2' = 1.36\omega_0$, which are in very good agreement with the values $T^* = 3T$, $\omega_1' = 1.64\omega_0$, and $\omega_2' = 1.36\omega_0$ from the experiments. At this nonlinearity, a symmetric class II instability (i.e. with $p = 0.5$) does exist, but is not dominant (setting $\langle p, q\rangle = \langle 0.5, 1.48\rangle$ yields $\sigma = 0.00433\mathrm{i}$). Hence, for a small range of parameters (again considering discrete $q$), it is possible for the dominant class II instability to result in oscillating crescent patterns similar to those observed in the experiments, which may help explain their selection. Although we have not been able to explain the emergence of oscillating patterns with exactly the same combination of parameters as reported by Collard & Caulliez (1999)($q = 1.48$ versus $q = 1.32$), the values are reasonably close. We find it particularly encouraging that the perturbation frequencies match so closely with the experiments.

This does not, however, account for the lack of the class I instability in the experiments. At this nonlinearity, the dominant class I instability corresponds to $\langle p, q\rangle = \langle 0.35, 0\rangle$, with $\sigma = -0.157 + 0.0156\mathrm{i}$, which is clearly stronger than the previously mentioned class II mode. It therefore seems that the class I instability may somehow be suppressed in the experiments (or alternatively, the class II instability artificially excited). The most obvious explanation for such a suppression is the use of a plastic film on the water surface. Collard & Caulliez (1999) indeed report that, in addition to preventing wave breaking, the film damps longitudinal wave modulations (also that it is used to 'isolate the three-dimensional wave pattern formation'). Bliven, Huang & Long (1986) also provide experimental evidence that the class I instability is suppressed by wind, which was also used in the experiments. As evidence of such a suppression, whatever the cause, we note that Collard & Caulliez (1999) report observing phase-locked L2 crescent patterns for waves exceeding a critical steepness $H/L = 0.16/\pi \approx 0.051$, far below where the class II instability is theoretically dominant. It is not clear why such a plastic film and/or the wind would suppress the class I modes more than their class II counterparts, though the experimental results seem to support this contention.

While this explanation is inevitably speculative, we do demonstrate a plausible scenario where class II instabilities resulting in oscillating crescent patterns similar to those observed in the experiments of Collard & Caulliez (1999) would indeed be likely to appear, while still working within the framework of existing theories. Additional experiments to gain a better understanding of the effects of the plastic film, as well as the wind, are probably necessary for a more complete understanding of the selection mechanism in the experiments.

## 6. Competition between unstable modes

We now investigate the initial competition up to the breaking point between various resonant interactions. Each simulation in this section uses the fourth-order smoothing filter applied at each time step, to have a minimal effect on the growth of the respective modes. Each simulation is run to the point of breakdown due to steepening of one or more wavefronts caused by the resulting instabilities. All harmonic analyses in this section use data from the final $4T$, to give an indication of the final evolved state.

### 6.1. *Competition between isolated class II modes*

We first investigate the direct competition between the dominant (symmetric) class II modes (§4) with the unsymmetric satellites (§5). We consider a simulation with carrier waves having $H/L = 0.096$ on a $1025 \times 17$ computational grid. The simulation uses a double perturbation with $k_{x1} = 1.5k_0$, $\omega_1' = 1.5\omega_0$ and $k_{x2} = k_0$, $\omega_2' = 1.32\omega_0$. Both

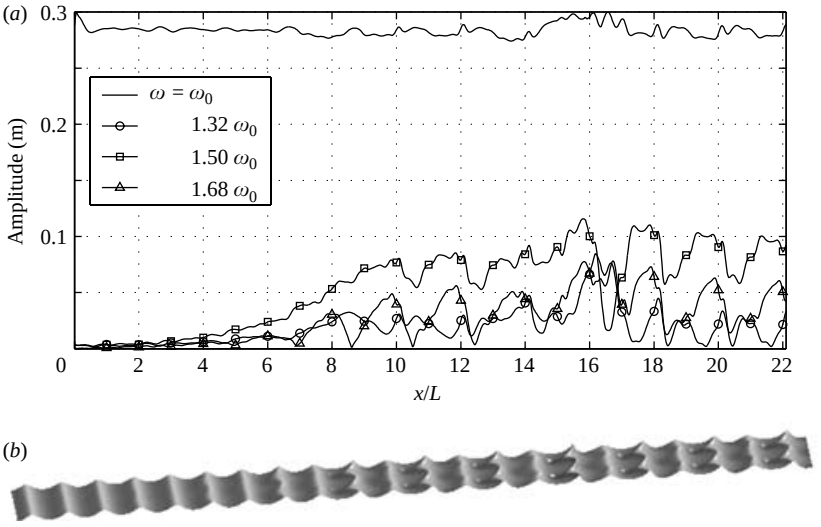


FIGURE 17. Computed (*a*) harmonic amplitudes and (*b*) free surface at $t = 24.4T$ for the simulation involving competition between symmetric (phase-locked) and unsymmetric (oscillating) class II instabilities with $H/L = 0.096$. In (*b*), the vertical scale is multiplied by two.

perturbations use $k_y = 1.32k_0$ and $\epsilon = 0.01$. Note that the second perturbation excites only one mode from each of the (oscillating) unsymmetric pairs (the others, i.e. with $k_x = 2k_0$ and $\omega' = 1.68\omega_0$, are free to evolve via the resonant quintet interactions). Both processes are excited with equivalent strength, however, and, in the absence of the other perturbation, simulations have shown that they develop to the expected patterns.

Figure 17(*a*) shows harmonic amplitudes corresponding to the various frequencies involved in the quintet resonant interactions. Clearly, both of the instabilities exhibit an initial growth, and as the strengths of the instabilities are nearly equivalent (see tables 3 and 4), neither dominates the other. Figure 17(*b*) shows the computed free surface at the end of the simulation involving the competing modes, where both instabilities are apparent. The overall pattern resembles the L2 pattern of § 4, however, clear deviations are noticeable at every other wavefront. Recall that the resonant interaction with the unsymmetric pairs results in oscillating crescents aligned in straight rows. These in turn cause an oscillating increase and decrease in the steepness of successive wave fronts – the L2 waves having the same momentary arrangement are steepened, while those having the opposite arrangement are diminished. This experiment demonstrates that multiple class II instabilities can develop simultaneously, with both contributing to the eventual breaking of the crescent waves. This is consistent with the findings of Annenkov & Shrira (1999, 2001), who also show the initial development of multiple class II instabilities.

### 6.2. *Competition between isolated class I and II modes*

We now use the model to investigate competition between isolated dominant class I and II instabilities. Three simulations are considered with incident waves having $H/L = 0.064$, 0.095 and 0.111. For each simulation, the dominant high-frequency component for both class I and II instabilities (see table 3) is excited with strength $\epsilon$. The class II perturbations use the $k_y$ values from table 1, while the class I perturbations

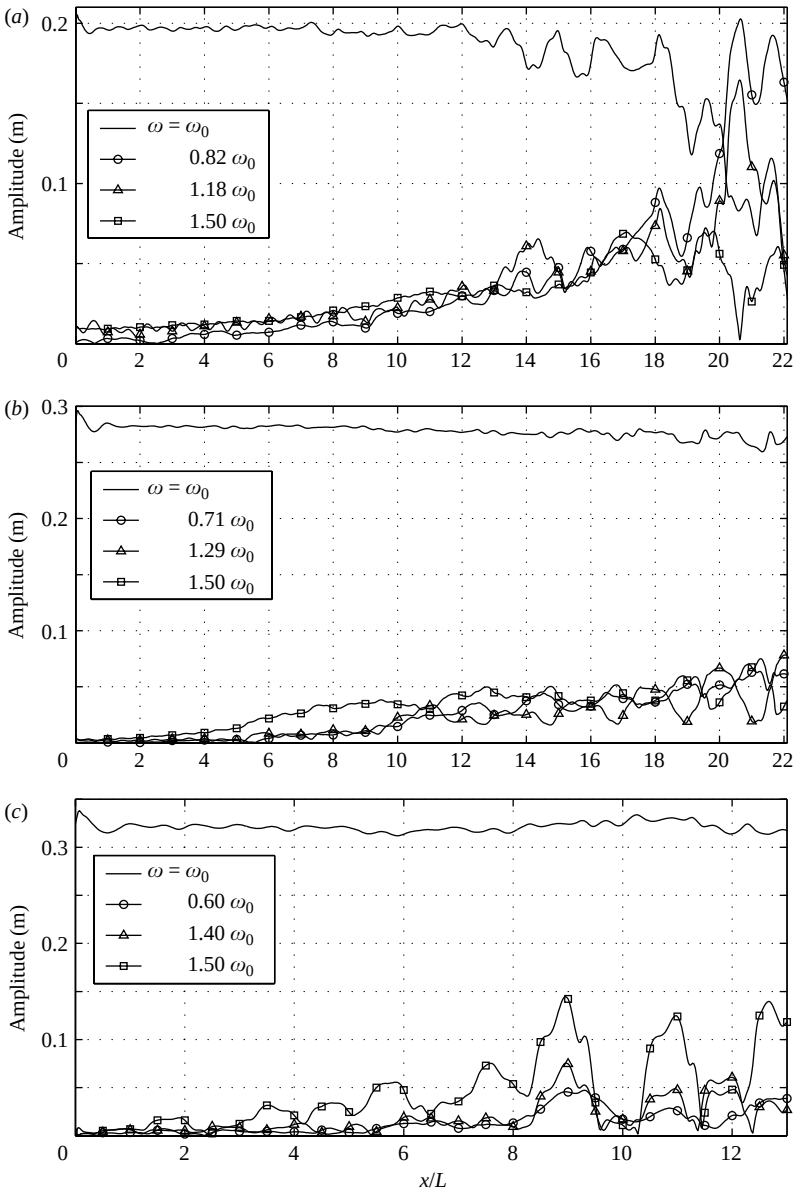


FIGURE 18. Computed harmonic amplitudes along $y = L_y/2$ for simulations with competing class I and II instabilities for (*a*) $H/L = 0.064$, (*b*) $H/L = 0.095$ and (*c*) $H/L = 0.111$.

use $k_y = 0$. The case with $H/L = 0.064$ uses $\epsilon = 0.05$, while the other two simulations use $\epsilon = 0.01$, all on a $1025 \times 17$ computational grid. The simulations with $H/L = 0.064$, 0.095 and 0.111 last for roughly $45T$, $21.25T$ and $13T$, respectively.

Figure 18 shows harmonic amplitudes along $y = L_y/2$ for the dominant frequencies involved in both the class I (quartet) and II (quintet) resonant interactions, while figure 19 shows computed free surfaces near the final state of each simulation. Figure 18(*a*) shows the case with $H/L = 0.064$, where the class I instability clearly dominates the class II instability, consistent with the expectation from the stability analysis of McLean (1982) (as well as our own analysis). In this case, the dominant

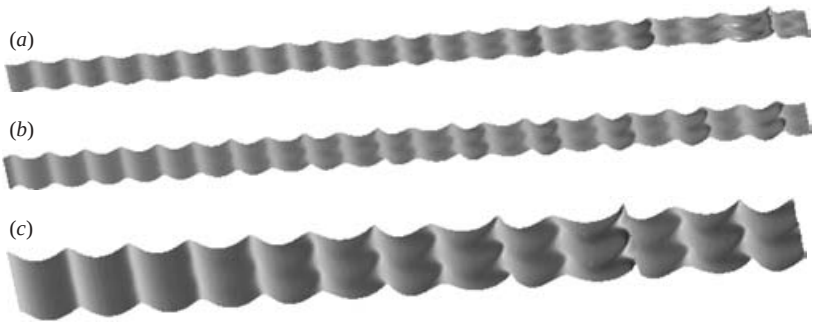


FIGURE 19. Computed free surfaces near the end state for simulations with competing class I and II instabilities for (*a*) $H/L=0.064$ at $t=43.75T$, (*b*) $H/L=0.095$ at $t=21.25T$ and (*c*) $H/L=0.111$ at $t=13T$. The vertical scale is multiplied by two.

lower class I sideband grows to roughly the same strength as the primary wave before eventually leading to breaking. Although the class II mode develops, it never reaches the considerable amplitudes of the class I modes. The free surface near the final model state is shown in figure 19(*a*), where the observed instability is only slightly three-dimensional. From table 3, this class I instability involves wavenumbers $k_{x1}=1.32k_0$ and $k_{x2}=0.68k_0$. Using simple superposition arguments, we can expect that the pattern will repeat itself with a length of $\approx 3L$, which matches that seen in figure 19(*a*) (upon close examination roughly every third wave near the end of the domain is steepened).

The case with $H/L=0.095$ is noticeably different. From table 3, the strength of the class I and II instabilities is similar at this nonlinearity. From the harmonic analysis in figure 18(*b*), it is seen that both instabilities grow in strength to roughly equivalent magnitudes. As might be expected, neither process dominates the other. The resulting free surface is shown in figure 19(*b*), where both two- and three-dimensional effects are apparent. The three-dimensional class II instability is instantly recognizable from the crescent forms. The two-dimensional class I instability can be distinguished, as it steepens roughly every other wavefront near the end of the domain. This is again consistent with the expectations from the wavenumbers involved, $k_{x1}=1.47k_0$, $k_{x2}=0.53k_0$.

The case with $H/L=0.111$ demonstrates relative dominance of the class II instability. The peak class I harmonic amplitudes shown in figure 18(*c*) are significantly lower than those of the class II mode, though they, too, develop. The computed free surface at the end of the simulation is shown in figure 19(*c*), where the resulting pattern is predominantly three-dimensional in nature, closely resembling the previous plot in figure 6(*b*) having the same nonlinearity. Minor two-dimensional effects are also apparent, steepening roughly every other wavefront near the end of the domain. These are of secondary importance, and are noticeably less pronounced than in figure 19(*b*).

### 6.3. *Competition of random disturbances*

All of the previously modelled crescent patterns have been generated using very deliberate two- and three-dimensional perturbations, as described in § 3. These have proved to be a very efficient means for generating isolated instabilities, however, it is perhaps not very representative of natural (or even laboratory) conditions resulting in such patterns. In this section, we therefore consider the nonlinear evolution of

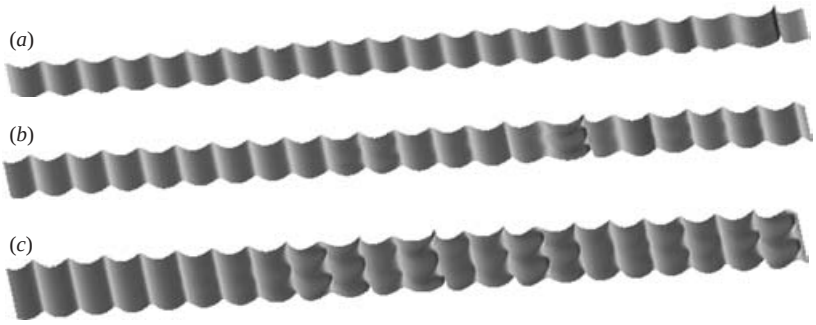


FIGURE 20. Computed wave patterns generated from simulations with random disturbances ($\epsilon = 0.02$) with (*a*) $H/L = 0.095$, $t = 34T$, (*b*) $H/L = 0.111$, $t = 23.75T$, and (*c*) $H/L = 0.127$, $t = 15.75T$. The vertical scale is multiplied by two.

randomly perturbed plane incident waves. Hence, the incident streamfunction solution values for the time stepping variables $\eta$, $\tilde{U}$ and $\tilde{V}$ are multiplied individually at each grid point by a factor $(1 + \epsilon\mu)$, where $\mu$ is a uniformly distributed random number between $-1$ and 1. We consider simulations using three nonlinearities $H/L = 0.095$, 0.111 and 0.127. Each simulation uses a $1025 \times 33$ computational grid (i.e. a full wavelength of the dominant transversal class II mode), with $\epsilon = 0.02$. Discretizations are again taken from table 1.

Computed free surfaces near the end of each simulation are shown in figure 20. Figure 20(*a*) shows the case with $H/L = 0.095$, which demonstrates a predominantly two-dimensional instability near the end of the computational domain. Minor three-dimensional effects are also apparent. Note that the class I instability does have a slightly larger linear growth rate than the corresponding class II instability at this nonlinearity (see McLean 1982, as well as table 3). The resulting free surface is much less three-dimensional than in figure 19(*b*) having the same nonlinearity. This could suggest that that the class II instability is suppressed more by the randomness than is the class I instability, at least at this nonlinearity (the suppression of the class I instability by randomness is demonstrated in Alber 1978). A more in-depth investigation would be necessary before making any firm conclusions on this matter, however.

Figure 20(*b*) shows the case with $H/L = 0.111$, which results in a predominantly three-dimensional steepening of the wave, again consistent with expectations from table 3. Both Su *et al.* (1982) and Melville (1982) report dominance of the three-dimensional instability at $H/L \approx 0.10$, thus, this is consistent with their observations. Two-dimensional effects are also clearly present, as every other wavefront around the crescent is slightly steepened. We also note that the emergence of the crescent at $x \approx 15L$ compares well with the observations of Melville (1982), who reports strong three-dimensional effects at $x \approx 10L$, as well as with Su *et al.* (1982), who report a first stage of wave evolution of $x \approx 19L$ (both with $H/L \approx 0.10$). We speculate that a continued evolution of the model beyond the breaking point might lead to clearer dominance of the class II instability at this nonlinearity.

Figure 20(*c*) shows the case with $H/L = 0.127$. Here, multiple L2-like patterns emerge starting at $x \approx 7L$. There is no noticeable indication of two-dimensional instabilities. We also call attention to the series of wavefronts starting at $x \approx 15L$ in figure 20(*c*), with successive fronts having minor peaks at $y = 0$, $L_y$ and $2L_y$. Such an arrangement deviates from the standard L2 pattern, and may be the beginnings

| Simulation | § | $H/L$ | $\epsilon$ | $N_s$ | $N_t$ | Preconditioning method | Iterations | $CPU$ [h] | $E \times 10^7$ [h] |
|---|---|---|---|---|---|---|---|---|---|
| L2 | 4.5 | 0.096 | 0.16 | 8721 | 5000 | Fourier | 12.7 | 4.45 | 1.02 |
| L2 | 4.3 | 0.105 | 0.16 | 8721 | 310 | Fourier | 12.4 | 0.32 | 1.18 |
| L2 | 4.3 | 0.105 | 0.16 | 8721 | 260 | Schur | 21.9 | 0.63 | 2.78 |
| L2 | 4.5 | 0.105 | 0.01 | 17,425 | 720 | Fourier | 7.9 | 1.13 | 0.90 |
| L2 | 4.5 | 0.105 | 0.01 | 17,425 | 720 | Schur | 16.9 | 3.03 | 2.42 |
| L2 | 4.5 | 0.131 | 0.05 | 8721 | 160 | Fourier | 14.2 | 0.20 | 1.43 |
| Oscillating | 5.1 | 0.096 | $2 \times 0.08$ | 8721 | 5000 | Fourier | 12.6 | 4.39 | 1.01 |
| Oscillating | 5.2 | 0.096 | $2 \times 0.08$ | 8721 | 5000 | Fourier | 12.0 | 4.30 | 0.99 |
| Competition | 6.2 | 0.064 | $2 \times 0.05$ | 17,425 | 1800 | Fourier | 8.1 | 2.65 | 0.84 |
| Competition | 6.2 | 0.111 | $2 \times 0.01$ | 17,425 | 530 | Fourier | 8.5 | 0.94 | 1.02 |
| Competition | 6.3 | 0.095 | 0.02 | 33,825 | 1370 | Fourier | 7.3 | 3.66 | 0.79 |
| Competition | 6.3 | 0.111 | 0.02 | 33,825 | 970 | Fourier | 8.4 | 2.89 | 0.88 |
| Competition | 6.3 | 0.111 | 0.02 | 33,825 | 970 | Schur | 17.9 | 8.99 | 2.74 |
| Competition | 6.3 | 0.127 | 0.02 | 33,825 | 640 | Fourier | 10.3 | 2.41 | 1.11 |
| Competition | 6.3 | 0.127 | 0.02 | 33,825 | 640 | Schur | 22.4 | 7.77 | 3.59 |

TABLE 5. Computational summary of selected crescent wave simulations. The reported iterations are the average in each simulation for solutions of $\boldsymbol{Ax} = \boldsymbol{b}$.

of potential L3- or L4-like patterns, as observed in Su *et al.* (1982) and Su (1982) (Melville 1982, also reports such deviations).

We finally mention a number of experiments involving the competition of various modes in Annenkov & Shrira (1999, 2001) using a weakly nonlinear model based on the Zakharov equation. Their experiments demonstrate sporadically occurring crescent patterns, occurring over long-term (i.e. $O(1000T)$) evolutions, whereas the experiments described here consider only the initial development to breaking, at significantly higher nonlinearities. Nevertheless, the experiments share some common tendencies. The results of Annenkov & Shrira (1999, 2001) also indicate the initial growth of multiple instabilities (as mentioned in § 6.1), as well as a tendency for significantly stronger modes to exhibit dominance over weaker instabilities. The vast difference in both time scales and nonlinearity make a more meaningful comparison difficult, however. The onset of breaking in each of the experiments presented here will most probably change the long-term evolution of the waves dramatically, making such sporadic patterns unlikely at the nonlinearities where the class II instability is dominant. For example, Su *et al.* (1982) report observing spilling crescent breakers for roughly $10L$, after which the wavetrains return to a more or less two-dimensional form. This process is later followed by a frequency downshift in the spectrum. The long-term fully nonlinear evolution of crescent waves remains relatively unstudied.

## 7. Computational efficiency

In this section, the issue of computational efficiency is briefly addressed. All previously described simulations have been run on a single Pentium 4 2.26 GHz processor with 1 GB of 266 MHz DDR-RAM. A summary of computational results for selected simulations is given in table 5. Here, $N_s$ refers to the number of spatial grid points, $N_t$ is the number of time steps, and

$$E = \frac{CPU}{N_s N_t} \tag{7.1}$$

is a measure of relative computational expense in terms of CPU time per grid point per time step (allowing for easy comparison of the various simulations). From this table it can be seen that the numerical solutions for $\boldsymbol{Ax} = \boldsymbol{b}$ (which are the dominant computational expense) in the Boussinesq model are robust, even in the most nonlinear situations. Modelling crescent waves is, in fact, demanding, as simulations are inevitably in deep water, require fairly refined grids, and are highly nonlinear – all factors contributing to the ill-conditioning of the matrix $\boldsymbol{A}$. Recall that the matrix-free Fourier space preconditioning method is limited to solving flat-bottom problems, owing to the assumption of constant coefficients in Fourier space. Therefore, some results using the generally applicable approximate Schur complement preconditioner developed in Fuhrman & Bingham (2004) are also included. These solutions can be seen to be somewhat less efficient (roughly by a factor of 3), but are still very acceptable. Solutions for the Boussinesq model have been shown by Fuhrman & Bingham (2004) to scale roughly linearly with $N_s$, which is generally confirmed through these simulations. The present Boussinesq model has proved to be an efficient method for the study of highly nonlinear water waves at reasonably large space and time scales – the simulations presented here take hours, not days, on a modern processor. This efficiency has allowed for a quantitative study of crescent wave patterns at significantly larger spatial and temporal scales than have been previously presented.

## 8. Conclusions

This paper presents a detailed numerical study of crescent (or horseshoe) water wave patterns using the fully nonlinear and highly dispersive Boussinesq formulation of Madsen *et al.* (2002, 2003). The numerical model uses the efficient solution strategies developed in Fuhrman & Bingham (2004). Herein, it is shown that the computed results for the most unstable phase-locked L2 crescent wave patterns compare both qualitatively and quantitatively well with observations, giving confidence in the model. The growth rate of the instability is shown to match closely with that predicted by the linear analysis of McLean (1982) near the inception. At later stages of the evolution, however, the growth is significantly accelerated when uninhibited by dissipation. The model results suggest that it is the dissipative effects due to wave breaking that ultimately counteract the unstable growth, leading to the relatively steady forms described in physical experiments. We also use the model to investigate the effects of variable nonlinearity on these patterns. We demonstrate that increases in the nonlinearity generally result in wider crescent patterns (as predicted by McLean 1982) with less pronounced tails. Through Fourier analysis of both time and space series, we confirm the quintet resonant interaction as the dominant physical process, involving the primary wave with a pair of symmetric satellites. A series of quadratic nonlinearities also force additional bound higher harmonics, giving definition to the crescent forms.

A numerical investigation of oscillating crescent waves, observed by Collard & Caulliez (1999), is also presented. The computed results provide a close match with the oscillation period observed in the physical experiments, and a detailed account of the complicated oscillation cycle is presented. Through direct numerical simulation, we also demonstrate distinct occurrences of L3 and L4 crescent patterns observed by Su *et al.* (1982) and Su (1982). These occur momentarily when the model is transitioning between various resonant interactions. The dominant physical processes in the oscillating crescent patterns are again demonstrated to be resonant quintet

interactions, involving the primary wave with two unsymmetric satellite pairs. The arrangement of the patterns in straight rows as observed by Collard & Caulliez (1999) is further shown to be merely a special case (visually) of these oscillating crescent waves, which, in general, do not have such an arrangement. A re-investigation into the stability analysis of McLean (1982) is undertaken, resulting in a quantitative explanation (including accurate predictions of the oscillation period) for each of the cases considered. A possible explanation of the selection of the oscillating patterns observed in the experiments is also provided.

Finally, the model is used to conduct a series of numerical experiments involving the competition of various unstable modes during the initial growth toward wave breaking. These include competition between isolated class II modes, between isolated class I and II modes, as well as with random (white noise) disturbances. The results show that multiple instabilities can grow simultaneously, provided that they are of similar strength, with each contributing to the eventual breaking of the waves. The computed results involving the random disturbances compare well with observations in wave tank experiments both in the form (i.e. two- or three-dimensional) and location of the initial instability. Deviations from the dominant L2 pattern also arise naturally, consistent with observations.

The computations presented in this work are the first examples of deep-water highly nonlinear (to the point of breaking) three-dimensional wave modelling with a high-order Boussinesq model. The model is generally applicable to variable-depth problems, and is shown to be an efficient computational method for the general study of highly nonlinear water waves at reasonably large space and time scales.

We would like to express our thanks to reviewers of this paper for their useful comments and suggestions. These have specifically inspired us to write § 5.4, correct table 3, and provide additional discussion on the role of dissipation in § 4.5. We also thank the Danish Center for Scientific Computing for providing invaluable supercomputing resources. This work was financially supported by the Danish Technical Research Council (STVF grant no. 9801635). Their support is greatly appreciated.

## REFERENCES

Alber, I. E. 1978 The effects of randomness on the stability of two-dimensional surface wavetrains. *Proc. R. Soc. Lond.* A **363**, 525–546.

Annenkov, S. Y. & Shrira, V. I. 1999 Sporadic wind wave horse-shoe patterns. *Nonlin. Proc. Geophys.* **6**, 27–50.

Annenkov, S. Y. & Shrira, V. I. 2001 Numerical modelling of water-wave evolution based on the Zakharov equation. *J. Fluid Mech.* **449**, 341–372.

Benjamin, T. B. & Feir, J. E. 1967 The disintegration of wave trains on deep water. Part 1. Theory. *J. Fluid Mech.* **27**, 417–430.

Bliven, L. F., Huang, N. E. & Long, S. R. 1986 Experimental study of the influence of wind on Benjamin–Feir sideband instability. *J. Fluid Mech* **162**, 237–260.

Collard, F. & Caulliez, G. 1999 Oscillating crescent-shaped water wave patterns. *Phys. Fluids* **11**, 3195–3197.

Craig, W. 2001 On the Badulin, Kharif and Shrira model of resonant water waves. *Physica* D **152–153**, 434–450.

Dommermuth, D. G. & Yue, D. K. P. 1987 A high-order spectral method for the study of nonlinear gravity waves. *J. Fluid Mech.* **184**, 267–288.

Fenton, J. D. 1988 The numerical solution of steady water wave problems. *Comput. Geosci.* **14**, 357–368.

Fuhrman, D. R. & Bingham, H. B. 2004 Numerical solutions of fully non-linear and highly dispersive Boussinesq equations in two horizontal dimensions. *Intl J. Numer. Meth. Fluids* **44**, 231–255.

Fuhrman, D. R., Bingham, H. B., Madsen, P. A. & Thomsen, P. G. 2004 Linear and non-linear stability analysis for finite difference discretizations of high-order Boussinesq equations. *Intl J. Numer. Meth. Fluids* **45**, 751–773.

Kharif, C. & Ramamonjiarisoa, A. 1986 Deep water gravity wave instabilities at large steepness. *Phys. Fluids* **31**, 1286–1288.

Kharif, C. & Ramamonjiarisoa, A. 1990 On the stability of gravity waves on deep water. *J. Fluid Mech.* **218**, 163–170.

Kusaba, T. & Mitsuyasu, H. 1986 Nonlinear instability and evolution of steep water waves under wind action. *Rep. Res. Inst. Appl. Mech. Kyushu University* **33**, 33–64.

Longuet-Higgins, M. S. & Cokelet, E. D. 1978 The deformation of steep surface waves on water II: Growth of normal-mode instabilities. *Proc. R. Soc. Lond.* A **364**, 1–28.

McLean, J. W. 1982 Instabilities of finite-amplitude water waves. *J. Fluid Mech.* **114**, 315–330.

McLean, J. W., Ma, Y. C., Martin, D. U., Saffman, P. G. & Yuen, H. C. 1981 Three-dimensional instability of finite-amplitude water waves. *Phys. Rev. Lett.* **46**, 817–820.

Madsen, P. A. & Agnon, Y. 2003 Accuracy and convergence of velocity formulations for water waves in the framework of Boussinesq theory. *J. Fluid Mech.* **477**, 285–319.

Madsen, P. A., Bingham, H. B. & Liu, H. 2002 A new Boussinesq method for fully nonlinear waves from shallow to deep water. *J. Fluid Mech.* **462**, 1–30.

Madsen, P. A., Bingham, H. B. & Schäffer, H. A. 2003 Boussinesq-type formulations for fully nonlinear and extremely dispersive water waves: derivation and analysis. *Proc. R. Soc. Lond.* A **459**, 1075–1104.

Melville, W. K. 1982 The instability and breaking of deep-water waves. *J. Fluid Mech.* **115**, 165–185.

Press, W. H., Teukolsky, S. A., Vetterling, W. T. & Flannery, B. P. 1992 *Numerical Recipes in FORTRAN: The Art of Scientific Computing*, 2nd edn. Cambridge University Press.

Saad, Y. & Schultz, M. H. 1986 GMRES: a generalized minimal residual algorithm for solving nonsymmetric linear systems. *SIAM J. Sci. Statist. Comput.* **7**, 856–869.

Savitzky, A. & Golay, M. J. E. 1964 Smoothing and differentiation of data by simplified least squares procedures. *Anal. Chem.* **36**, 1627–1639.

Shrira, V. I., Badulin, S. I. & Kharif, C. 1996 A model of water wave 'horse-shoe' patterns. *J. Fluid Mech.* **318**, 375–404.

Shrira, V. I., Badulin, S. I. & Voronovich, A. G. 2000 EM scattering from sea surface in the presence of wind wave patterns. *Intl Geosci. Remote Sensing Symp.* vol. 2, pp. 926–928.

Skandrani, C. 1997 Contribution à l'étude de la dynamique non linéaire des champs de vagues tridimensionnels en profondeur infinie. PhD thesis, Université de la méditerranée, Aix-Marseille II, Marseille, France.

Su, M. Y. 1982 Three-dimensional deep-water waves. Part 1. Experimental measurement of skew and symmetric wave patterns. *J. Fluid Mech.* **124**, 73–108.

Su, M. Y., Bergin, M., Marler, P. & Myrick, R. 1982 Experiments on nonlinear instabilities and evolution of steep gravity-wave trains. *J. Fluid Mech.* **124**, 45–72.

Xue, M., Xü, H., Liu, Y. & Yue, D. K. P. 2001 Computations of fully nonlinear three-dimensional wave–wave and wave–body interactions. Part 1. Dynamics of steep three-dimensional waves. *J. Fluid Mech.* **438**, 11–39.

Zakharov, V. E. 1968 Stability of periodic waves of finite amplitude on the surface of a deep fluid. *J. Appl. Mech. Tech. Phys.* **9**, 190–194.